

THE ACCRETION DISK WIND IN THE BLACK HOLE GRO J1655–40

J. M. MILLER¹, J. RAYMOND², C. S. REYNOLDS³, A. C. FABIAN⁴, T. R. KALLMAN⁵, J. HOMAN⁶

Subject headings: Black hole physics – relativity – stars: binaries (GRO J1655–40) – physical data and processes: accretion disks

Draft version October 31, 2018

ABSTRACT

We report on simultaneous *Chandra*/HETGS and *RXTE* observations of the transient stellar-mass black hole GRO J1655–40, made during its 2005 outburst. *Chandra* reveals a line-rich X-ray absorption spectrum consistent with a disk wind. Prior modeling of the spectrum suggested that the wind may be magnetically driven, potentially providing insights into the nature of disk accretion onto black holes. In this paper, we present results obtained with new models for this spectrum, generated using three independent photoionization codes: XSTAR, Cloudy, and our own code. Fits to the spectrum in particular narrow wavelength ranges, in evenly spaced wavelength slices, and across a broad wavelength band all strongly prefer a combination of high density, high ionization, and small inner radius. Indeed, the results obtained from all three codes require a wind that originates more than 10 times closer to the black hole and carrying a mass flux that is on the order of 1000 times higher than predicted by thermal driving models. If seminal work on thermally-driven disk winds is robust, magnetic forces may play a role in driving the disk wind in GRO J1655–40. However, even these modeling efforts must be regarded as crude given the complexity of the spectra. We discuss these results in the context of accretion flows in black holes and other compact objects.

1. INTRODUCTION

Accretion disks around black holes in X-ray binaries are sure to have a role in nearly every aspect of such systems, from radiative energy release to jet production. Black hole disks can potentially even be used to reveal black hole spin, Lense-Thirring precession, and other aspects of General Relativity. However, it is extremely difficult to obtain clean measurements of the thermal continuum emission from black hole disks. Absorption along the line of sight, uncertainties in the nature and degree of simultaneous hard X-ray emission, and uncertainties in parameters like distance, inclination, mass accretion rate, and the effects of radiative transfer through disk atmospheres are just some of the difficulties associated with studies of the disk continuum. Fortunately, we can improve our understanding of black holes and their accretion disks by focusing on timing studies, emission lines broadened by orbital motions, and disk winds (e.g. Strohmayer 2000, Miller 2007, Proga 2003, Miller et al. 2006). Of these, disk winds may seem to be the least telling, but winds can in fact reveal a great deal about the nature of disks.

Accretion disks transfer matter radially inward while transporting away angular momentum (for background, see Frank, King, & Raine 2002). While theoretical work on this topic is quite advanced, observational constraints are relatively poor, especially in the case of black hole disks. Internal magnetic viscosity may drive disk accretion (e.g. Shakura & Sunyaev 1973, Balbus & Hawley 1991), and could give rise to slow, dense winds originating close to the black hole (e.g. Proga 2003). An optically-thick blackbody-like spectrum should also result from this process (Shakura & Sunyaev 1973), though this signature

is a generic prediction of any internal viscosity mechanism. Alternatively, rigid magnetic fields may transport angular momentum by allowing some matter to be accelerated along field lines (Blandford & Payne 1982; see also Spruit 1996). The resulting winds may be clumpy, and should show significant rotation. A characteristic thermal disk spectrum is not a requirement in such a scenario.

Clearly showing that either magnetic process is at work in accreting black holes would shed important new light on accretion disk physics. However, magnetic fields are not the only means of driving winds in accreting systems, nor the most readily observable. Radiation pressure can effectively drive moderately ionized winds, due to spikes in the cross section due to certain UV transitions (e.g. Cordova & Mason 1982, Proga, Stone, & Drew 1998). Compton heating of the accretion disk by a central source of X-rays can raise the local gas temperature to the escape velocity, and drive thermal winds in accreting systems (Begelman, McKee, & Shields 1983, Woods 1996). Differentiating magnetic winds from radiatively and thermally-driven winds is largely a question of accurately determining the launching radius, density, and geometry of the wind. Relative to radiatively and thermally-driven winds, magnetic winds can originate closer to the black hole and can have significantly higher density (e.g. Proga 2003). Accurate modeling of sensitive high resolution spectra with photoionization codes can determine these parameters with a fair degree of confidence.

In FU Ori stars, spectra reveal clear evidence of magneto-centrifugal winds (Calvet, Hartmann, & Kenyon 1993), demonstrating that such winds are important in at least some accreting systems. Evidence for magnetic winds from accretion disks

¹Department of Astronomy, University of Michigan, 500 Church Street, Ann Arbor, MI 48109, jonmm@umich.edu

²Harvard-Smithsonian Center for Astrophysics, 60 Garden Street, Cambridge, MA 02138

³Department of Astronomy, University of Maryland, College Park, MD 20742

⁴Institute of Astronomy, University of Cambridge, Madingley Road, Cambridge CB3 0HA, UK

⁵Laboratory for High Energy Astrophysics, NASA Goddard Space Flight Center, Code 662, Greenbelt, MD 20771

⁶MIT Kavli Institute for Astrophysics and Space Research, 70 Vassar Street, Cambridge MA, 02139

around compact objects has been lacking until recently. Observations of one white dwarf system reveal that radiative driving is insufficient, leading to the suggestion that magnetic pressure may be important (Mauche & Raymond 2000). In at least one Seyfert AGN, there is some indirect evidence for a magnetocentrifugal wind (Kraemer et al. 2005). A turning point may have come with a *Chandra*/HETGS observation of the stellar-mass black hole GRO J1655–40 in outburst. Modeling of that spectrum suggested a slow, very dense wind originating close to the black hole. The radius and density parameters and inferred geometry are all suggestive of a wind driven by magnetic forces, and may signal a wind driven by the Poynting flux generated by internal magnetic viscosity (Miller et al. 2006; hereafter, Paper I). It is only because all other viable driving mechanisms appear to be ruled-out that magnetic driving must be considered; we cannot measure Zeeman splitting in X-rays to directly probe the magnetic field. Applying the same logic, the winds detected in the stellar-mass black hole candidates H 1743–322 (Miller et al. 2006b) and 4U 1630–472 (Kubota et al. 2007) may also be driven magnetically. However, better-known driving mechanisms are less rigidly excluded in these sources.

GRO J1655–40 is a particularly interesting and well-observed black hole X-ray binary. Outbursts from this transient were previously observed in 1994 and 1996. The apparently superluminal jets observed in radio band put GRO J1655–40 into the “microquasar” category (see Hjellming & Rupen 1995). Of the approximately 20 X-ray binaries in which dynamical constraints demand a black hole primary (see McClintock & Remillard 2006), the parameters of GRO J1655–40 are best understood. The binary is likely 3.2 kpc distant, and appears to consist of a $7.0 \pm 0.2 M_{\odot}$ black hole orbiting a $2.3 M_{\odot}$ F3 IV – F6 IV companion star in a 2.6-day orbit (Orosz & Bailyn 1996). The binary is likely viewed at an inclination of 67° , although the inner disk may be viewed at an inclination as high as 85° (Hjellming & Rupen 1995). An alternative mass and distance have recently been suggested (Foellmi et al. 2006); however, these values would not allow the companion star to fill its Roche lobe (J. Orosz, private communication). The precision with which these parameters are known is of tremendous help in efforts to estimate parameters like black hole spin, the mass accretion rate, and other facets of the system and accretion flow.

Herein, we report on the results of more extensive modeling of the disk wind spectrum of GRO J1655–40. In addition to simple phenomenological modeling of the spectrum and order-of-magnitude estimates regarding the nature of the wind, we have developed new photoionization models. The code described in Raymond (1993) and Miller et al. (2006b) agrees well with the more widely used XSTAR and Cloudy models. Here, we use XSTAR and Cloudy because those codes contain the most recent atomic rates and because they are thoroughly documented and familiar to many astronomers. Moreover, these codes now allow users to develop grids of models that may be implemented into fitting packages like XSPEC and ISIS, so that direct spectral fitting and direct χ^2 minimization techniques can be employed to constrain the nature of complex spectra. Netzer (2006) described models for the wind in GRO J1655–40 consistent with thermal driving, and those parameters serve as an important point of reference in our analysis. Although some of the most extreme parameters reported in Miller et al. (2006b) can be slightly relaxed, magnetic driving is still required if present models of thermal driving are accurate. The inner radius at which the wind must be produced is at

least an magnitude smaller than is predicted by analytical and numerical thermal wind models, and the mass outflow rate is at least three orders of magnitude greater than predicted by the same models.

2. OBSERVATIONS AND DATA REDUCTION

Chandra observed GRO J1655–40 on 2005 April 1, starting at 12:41:44 (UT, or MJD 53461.53); 44.6 ksec of net exposure time were obtained after standard filtering. The High Energy Transmission Grating Spectrometer (HETGS) was used to disperse the incident flux onto the ACIS-S array. The array was operated in “continuous-clocking” because the nominal 2.8 ms frametime of this mode prevents photon pile-up. In order to limit telemetry saturation and the loss of frames, we used a gray filter in the region around the aimpoint to record only one in 10 incident zeroth order photons. Recording some zeroth order photons is critical to establishing the wavelength grid in later reduction.

The *Chandra* observation was processed using the CIAO reduction and analysis suite, version 3.2.2. The evt1 file was filtered to accept only the standard event grades, to accept only events from the nominal good-time intervals, and to reject events from bad pixels. The “destreak” tool was run to remove the effects of streaking on the ACIS CCDs. Spectra were extracted using the default settings for the tools “tg_resolve_events” and “tgextract”. We used canned rmf files to produce arfs via the “fullgarf” tool. For final analysis, first-order HEG spectra and arfs, and first-order MEG spectra and arfs, were added using the tool “add_grating_spectra”. (As any real spectral line within a band covered by multiple first-order spectra must be present in *all* spectra, the individual first-order spectra were frequently checked during the line identification process to select only robust lines.) The instrumental configuration and the reduction procedure outlined above are fully consistent with prior observations and analyses of observations made in this mode; for additional discussion and context please see Miller et al. (2004, 2006b) and Cackett et al. (2007).

RXTE observed GRO J1655–40 simultaneously with *Chandra*, to provide improved constraints on the broad-band X-ray continuum emission and flux variability. A 12.6 ksec *RXTE* observation was obtained starting on 2005 April 1 at 13:47:12 (UT). The tools and packages in the HEASOFT version 6.04 suite were used to reduce and analyze all *RXTE* data. Of the independent proportional counter units in the *RXTE*/PCA, PCU-2 is the best-calibrated. We therefore restricted our spectral reduction and analysis to this detector. Spectra from PCU-2 were extracted from data taken in Standard-2 mode, providing full coverage of the 2.0–60.0 keV bandpass in 129 channels every 16 seconds. Data from all of the Xe gas layers were combined. The combined PCA spectra were corrected for detector deadtime. Background spectra were made using the tool “pcabackest” and the appropriate bright-source background files. Redistribution matrix files (rmfs) and ancillary response files (arfs) were made and combined into a single file using the tool “pcarsp”. Fits to spectra of the Crab reveal deviations from a simple power-law at the 0.6% level; we therefore added 0.6% systematic error to all PCA bins using the tool “grppha” prior to spectral analysis (this is common practice; e.g. Miller et al. 2006b). Spectra from HEXTE-A cluster were also reduced and analyzed. Spectra were made from standard archive mode data, which has a nominal time resolution of 32 seconds and covers the 10–250 keV band with 61 channels. All

spectra were background-subtracted and deadtime-corrected using the standard procedures. We fit spectra from PCU-2 in the 3–25 keV band, and spectra from HEXTE-A above 20 keV, as the instruments are well calibrated in these ranges.

Spectra obtained with *RXTE* were analyzed using XSPEC version 11.3.2 (Arnaud 1996). Joint fits to the simultaneous *RXTE* and broad-band *Chandra* spectra were also made using XSPEC. Detailed analysis of *Chandra* spectra involving both phenomenological and photoionization modeling of the absorption was done using ISIS version 1.3.3 (Houck & Denicola 2000). In the analysis that follows, errors on continuum parameters are 90% confidence errors, and errors on line parameters and photoionization model parameters are 1σ errors.

3. PRELIMINARY ANALYSIS

3.1. The 2005 Outburst Profile

RXTE monitored the 2005 outburst of GRO J1655–40 at an exceptionally high cadence, providing an excellent view of the source behavior. In this section, we briefly note some general points. All of the spectra, lightcurves, and power spectra from the large monitoring campaign were obtained using the procedure outlined above and the methods described in Homan (2005). In order to plot the source lightcurve in Crab units, the source count rate was converted using the fact that the Crab gives 2250 counts per second per PCU. This conversion is inexact because the Crab has a well-known power-law spectrum, whereas black holes can have more complex spectra dominated by thermal emission. The hardness curve was produced by taking the ratio of count rates in the 10–20 keV and 3–6 keV bands. Finally, the rms variability curve was generated by making Fast Fourier Transforms of each observation using the method detailed in Homan et al. (2005), and obtain the fractional rms in the 128^{-1} –64 Hz band from the rms normalized and Poisson subtracted power spectra.

Figure 1 plots the resulting lightcurve, spectral hardness curve, and fractional variability curve. The *Chandra* and *RXTE* observations analyzed in this work were obtained at the start of the 2005 outburst of GRO J1655–40, during a complex rise phase spanning roughly 100 days. Black hole transients exhibit periods of rather distinctive and correlated multi-wavelength phenomena; these are sometimes called “states” (for a review, see the discussion of states in McClintock & Remillard 2006). The “high/soft” or “thermal dominant” state is typified by low fractional variability and a very soft (disk-dominated) spectrum. The *Chandra* spectra analyzed in this work were clearly obtained in the disk-dominated “high/soft” or “thermal dominant” state.

3.2. Continuum Spectroscopy

The observed continuum spectra are very soft. This fact, coupled with the low effective area of *Chandra* above approximately 8 keV, makes it difficult to accurately characterize non-thermal components that are either very steep or very weak using *Chandra* alone. Conversely, *Chandra* is better suited for determinations of both disk parameters and the equivalent neutral hydrogen column density along the line of sight than *RXTE*. We therefore determined the continuum by using the strengths of each observatory.

A precise and detailed characterization of the continuum and any disk reflection features (for a review, see Miller 2007) is beyond the scope of this paper. However, a robust determination of the continuum is possible with simple fiducial models

that allow the broad-band source luminosity to be estimated accurately. We fit all of the simultaneous spectra with a phenomenological model consisting of disk blackbody (Mitsuda et al. 1984) and power-law components, modified by absorption in the ISM using the “phabs” model. An overall constant was allowed to float between the components to account for residual calibration errors. Fits to MEG spectra were restricted to the 0.65–5.0 keV (2.5–19Å) band, and fits to HEG spectra were restricted to the 1.2–10.0 keV (1.2–10Å) band as the HETGS is best calibrated for broad-band fitting in these windows.

We assumed the standard column density along this line of sight in all fits ($N_H = 7.4 \times 10^{21} \text{ cm}^{-2}$, Dickey & Lockman 1990). Fits to the *RXTE* spectra suggest a disk-dominated spectrum, with a power-law index of $\Gamma = 3.54(1)$. In fits to the *Chandra*/HETGS spectra, we then fixed this power-law index and derived better constraints on the disk flux. Fits with a this power-law index and a disk component give an inner disk color temperature of $kT = 1.35(1) \text{ keV}$. The total model gives an unabsorbed 0.65–10.0 keV flux of $4.0(1) \times 10^{-8} \text{ erg cm}^{-2} \text{ s}^{-1}$ ($L_X = 5.0(1) \times 10^{37} \text{ erg s}^{-1}$). The errors are also fiducial because the overall fit is poor ($\chi^2/\nu > 28$) owing to the strong absorption lines in the *Chandra* bandpass and calibration uncertainties. However, the continuum spectrum is characterized very well by these fits. It is worth noting that the source is not clearly detected above 30 keV. This is consistent with the observation occurring in a “high/soft” or “thermal dominant” state, as noted above.

4. DETAILED ANALYSIS AND MODELING OF THE DISK WIND

The absorption spectrum revealed in our observations of GRO J1655–40 is extremely complex. This necessitates a careful, step-wise approach to characterizing the spectrum and the properties of the observed disk wind. Both the analysis itself and its presentation are geared toward organizing complex results from complex models in the most clear and unbiased way possible.

First, we present a simple phenomenological description of the absorption spectrum using independent Gaussian models for each of the lines. We then note some of the basic wind properties that can be inferred even with such basic modeling. Special attention is given to some specific properties of the wind. From there, we detail efforts to model the wind using independent photoionization codes. The different codes are employed to mitigate biases that might be peculiar to just one code. To prevent biases related to wavelength selections and fitting ranges, we made fits to specific wavelength regions, to a broad wavelength band, and in evenly-spaced wavelength slices. The results of these steps are reported and discussed below.

4.1. Phenomenological Line Modeling

Closely following the procedure in Paper I, we made fits to the *Chandra*/HETGS spectra in 2–4 Å slices using fiducial local continuum models and simple Gaussian functions to describe the absorption lines. The strengths of this procedure are that it is model-independent and that it is useful for identifying lines, measuring wavelength (velocity) shifts, and crudely estimating line strengths. We detect 90 absorption lines significant at the 5σ level of confidence or higher. A boot-strap approach of searching for strong lines from abundant elements and then associated weaker lines succeeds in identifying 76 of the lines. The species observed span 32 charge states.

The fits are shown in Figure 2 and Figure 3, and the line pa-

rameters and identifications derived are given in Table 1 and Table 2. The lines were identified based on the wavelengths given in standard spectroscopic references including Verner, Verner, & Ferland (1996), the NIST Atomic Spectra Database, and Nahar & Pradhan (1999). Oscillator strengths were also taken from these references. The column densities given in Table 1 and Table 2 were calculated assuming that all lines were generated on the linear part of the curve of growth (see Spitzer 1978).

The absorption lines detected show blue-shifts in the range of 300–1600 km/s, signaling an outflow. No clear emission lines are detected in the spectrum, strongly suggesting that the outflow does not fill the entire volume available (see below). The detection of Fe XXII absorption lines at 11.770Å and 11.920Å is especially fortuitous, as these lines serve as density diagnostics with a sensitivity comparable to He-like line triplets (Mauche, Liedahl, & Fournier 2003).

There are a few major shortcomings of this simple phenomenological approach. First, some of the lines observed are likely to be saturated. This can be seen in the fact that trends in equivalent width and column density for a given ion do not follow that expected based on oscillator strength. Gaussian line models are likely to be inadequate when lines are saturated as this functional form misses power in the wings of a line; a Voigt profile is the right functional form in such circumstances. For these reasons, the column densities reported in Tables 1 and 2 should be regarded with caution. For the strongest lines expected from each charge state, this procedure can even complicate measures of velocity widths and velocity shifts. The Fe XXV He- α line at 1.850Å is not observed to have a blue-shift, for instance, and this is likely an effect of saturation making it difficult to accurately estimate velocities. Finally, this procedure is not guided by a self-consistent physical picture – all of the Gaussian models are independent and not governed by realistic global plasma parameters.

4.2. Basic Wind Properties

The binary is likely viewed at an inclination of 67° (Orosz & Bailyn 1996). Thus, our line of sight is already close to the plane of the disk. However, if we assume that the radio jet axis coincides with the black hole spin axis, and that the inner disk is anchored perpendicular to that axis (Bardeen & Petterson 1975, Blandford & Znajek 1977), then we may view the *inner* disk at an inclination of 85° (Hjellming & Rupen 1995). This might suggest a viewing angle of only 5° above the accretion disk, but the need to see over the flared outer edge of the disk suggests a lower limit of 6° (Vrtilek et al. 1990). An upper limit on the vertical extent of the gas of 12° can be derived from the lack of emission features in the spectrum (see Paper I).

Thus, simple geometrical arguments suggest that the observed absorption is an outflow along the plane of the disk, or at least an outflow with a high density along the plane of the disk. A hot central corona of the kind sometimes invoked to account for hard X-ray emission in black holes could not supply the range of charge states or column densities observed. Moreover, because the mass donor companion star in GRO J1655–40 is a low mass star (Orosz & Bailyn 1996), the observed wind must be expelled from material in the accretion flow. An accretion disk wind is thus the only viable explanation for the observed absorption spectrum.

In X-ray binaries with high mass companions, absorption can change with the orbital phase of the binary as the viewing angle to the X-ray source through the companion wind changes.

Such a variation is not expected in a low-mass X-ray binary like GRO J1655–40. Indeed, when the observation is divided into time segments, the resulting spectra show that the lines observed are effectively constant across the entire observation. Similarly, no significant variability is seen when spectra selected from intervals of low and high count rates are compared. These findings signal that the wind is not likely due to irradiation of a phase-dependent structure. Varying degrees of absorption were seen in independent observations with *XMM-Newton*, but those variations were driven by changes in the X-ray state of the source and dramatic changes in the ionizing flux (Diaz Trigo et al. 2007, Sala et al. 2007).

More importantly, the lack of strong variability in the spectrum suggests that partial covering of the central engine along the line of sight is unlikely. Partial covering can occur when an absorber has significant and variable density structure. The density structures must be small compared to the central engine, and so “clumps” of dense material must be invoked (the winds of massive stars are known to be clumpy, for instance). If the wind in GRO J1655–40 was concentrated into clumps, they would travel on the order of 10^{12} cm during our observation, assuming the lowest values of the blue-shifts observed (300 km/s). That distance is of the same order of magnitude as the size of binary system itself. If the wind were clumpy, blobs would easily move into and out of our line of sight during the observation, strongly affecting the degree of absorption observed. The absence of strong variability makes partial covering unlikely in GRO J1655–40.

4.3. Differentiating Wind Driving Mechanisms

Under the right conditions, radiation pressure can efficiently drive winds. At moderate ionization parameters, the cross section for certain UV line transitions greatly increases, and allows momentum to be transferred to the wind effectively. A strong source of UV radiation and moderately ionized gas are the only real requirements. Thus, radiation pressure is the means by which winds are driven from O stars, and it is undoubtedly important in driving some winds from accreting white dwarfs and AGN. However, for ionization parameters of $\xi = 10^3$ and higher, radiation pressure supplies little additional driving force (e.g. Proga, Stone, & Kallman 2000). The fact that the UV zone of the disk is not the most central zone in X-ray binaries also makes it difficult to drive winds through line force unless the wind density is extremely high (Proga & Kallman 2002).

A strong majority of the lines observed in GRO J1655–40 are from He-like and H-like charge states; there are very few L shell transitions and very few UV transitions remaining. Even from the crude analysis detailed above, then, it is clear that radiation pressure cannot drive the wind observed. The detailed photoionization modeling outlined below further confirms this finding.

Thermal winds can originate when the (flared) outer accretion disk is irradiated by the central X-ray source. If Compton heating of the disk surface is able to raise the gas temperature to that corresponding to the local escape speed, the heated material can flow out of the system. Both analytic (Begelman, McKee & Shields 1983; BMS) and numerical (Woods et al. 1996) models of thermally driven winds from X-ray illuminated accretion disks have been developed. The numerical models eliminate the most serious approximations of BMS, namely the simplified flow geometry and the neglect of the photoionization heating and collisional excitation cooling that dominate in the gas that produces the observed absorption lines. Nevertheless,

the numerical models agree quite well with the analytic ones.

The models predict that a thermally driven wind can arise outside $0.1 R_C$ (BMS) or $0.2 R_C$ (Woods et al. 1996). The Compton radius is given by $R_C = (1.0 \times 10^{10}) \times (M_{BH}/M_\odot)/T_{C8}$ (where T_{C8} is the Compton temperature in units of 10^8 K). In Paper I, we used the gas temperature in this equation; using the Compton temperature derived in the photoionization models described below, we find $T_C \simeq 1.4 \times 10^7$ K and $R_C \simeq 10^{11.7}$ cm, in agreement with an independent analysis by Netzer (2006).

Even if the gas were beyond $0.1 R_C$, the density predicted by the thermal wind models is far lower than observed. Equation 4.8 of Woods et al. (1996), or their Figure 16 scaled from a $10^8 M_\odot$ black hole to a $7 M_\odot$ black hole, predict the peak mass loss rate per unit area. For an ionizing spectrum that gives a Compton temperature close to that found in our models or Netzer's, the maximum is $6 \times 10^{-6} \text{g cm}^{-2} \text{s}^{-1}$, compared with an observed mass flux of about $10^{-2} \text{g cm}^{-2} \text{s}^{-1}$. Woods et al. find that the flow is nearly vertical between $0.1 R_C$ and R_C , and the high inclination angle means that the actual speed is considerably larger than the line-of-sight component, so the predicted density is still smaller.

If a wind originates significantly closer to the black hole than is predicted by thermal driving models, and/or if the density observed is significantly above the predictions of the same models, magnetic driving is the only viable means of powering a disk wind. Density can be deduced from density-sensitive line ratios, and from photoionization modeling to a lesser extent. The inner radius at which absorption is observed to occur can be derived from photoionization modeling. Differentiating magnetic and thermal driving mechanisms, then, is largely a question of accurately determining the radius and density of the wind observed.

4.4. On the density of the wind

The brief discussion above makes it clear that accurately estimating the density of a disk wind is critical to understanding its nature. In emission line spectra, density is often constrained using He-like triplet lines, but the observed spectrum lacks both emission lines and clear evidence of intercombination and forbidden lines. However, Fe XXII absorption lines are present in the spectrum (see Figure 3, and Table 2). The relative populations of the fine structure states of the ground level of Fe XXII, $2p^2 P_{1/2}$ and $2p^2 P_{3/2}$, provide a density diagnostic at $n_e \sim 10^{12} - 10^{15} \text{cm}^{-3}$ (Mauche et al. 2003).

We have measured the equivalent widths of the Fe XXII lines using a common continuum for both lines and adding the constraint that the separation equal the known separation of these lines. This methodology is slightly revised and improved from Paper I, and it provides a tighter constraint on the line ratio. The new equivalent widths are 16.0 ± 0.6 and $12.2 \pm 0.7 \text{m}\text{\AA}$ for the 11.77 and 11.92 \AA lines, respectively. Taking the oscillator strengths and the effects of slight saturation into account, this implies $0.62 \leq n_2/n_1 \leq 0.76$, where n_2 and n_1 are the populations of the $J=3/2$ and $1/2$ states, respectively. Figure 4 shows the population ratio computed with CHIANTI (Landi et al. 2006) for temperatures between 10^5 and $10^{6.3}$ K, corresponding to the upper and lower stable temperature branches of the photoionization equilibrium. We note that radiative excitation of permitted lines could in principle increase n_2/n_1 . However, even if the very steep power law extends to wavelengths near 100 \AA , radiative excitation only makes a significant dif-

ference if the gas is located within about 10^9 cm of the black hole.

In Paper I, we considered both the high and low temperature limits to be acceptable possibilities, but it seems likely that if the Fe XXII were formed in the low temperature branch, other lower Fe ions would also be present. Therefore, it appears that the $1 - 2 \times 10^6$ K range of the upper branch as predicted by our models is appropriate (this was confirmed independently using CLOUDY and XSTAR), and the density is near to or within the range $13.6 \leq \log(N_e) \leq 13.8$. It is reasonable to expect that the most ionized part of the wind originates close to the black hole, and indeed most of the lines observed are from He-like and H-like charge states. If there is any fall in density with radius, then the density range quoted here might be regarded as an effective lower bound.

In contrast, Netzer (2006) presents two closely-related models for the disk wind in GRO J1655-40 that are consistent with thermal driving. The density range found above is 3-6 times the densities at the inner edges of the models described by Netzer (2006). The densities of those models decrease with radius, so the average densities are around half the densities at the inner edge. The density distributions for both models predict column densities N_2/N_1 close to 0.1, a factor of 7 below the observed value.

The models developed by Netzer (2006) are partially motivated by a different interpretation of the Fe XXII lines. A brief comparison to those models provides a useful mechanism for discussing the Fe XXII lines and density determination in more detail. The Netzer models assume that the 11.77 \AA line is saturated, and that the absorbing gas covers only 75% of the X-ray emitting region. To support this interpretation, Netzer suggests that two unidentified lines at 11.54 and 11.42 \AA are Fe XXII lines with smaller oscillator strengths. With wavelengths from CHIANTI (Young et al. 2003) it is more logical to identify the line at 11.47 \AA with a blue-shifted Fe XXII line at 11.51 \AA . In that case, the equivalent widths of these lines from the lower fine structure level but with small oscillator strengths would be comparable to that of the 11.92 \AA line, and this is more or less what is observed (see Table 2).

The latter interpretation cannot be correct, however, because it also implies that the $2s^2 2p^2 P_{1/2} - 2s^2 4d^2 D_{3/2}$ line at 8.97 \AA should also be stronger than the 11.51 \AA line. An unidentified line at 8.96 \AA is listed in Paper I with an equivalent width of 2.6 $\text{m}\text{\AA}$ (also see Table 2). This is exactly what is predicted given the oscillator strengths from CHIANTI (Young et al. 2003) and the column density derived from the 11.77 \AA line under the assumption that both are *optically thin*. It is at least a factor of 4 smaller than the value expected from Netzer's suggestion of saturation and a partial covering factor. It is likely that the 8.96 \AA line is Fe XXII and that the features near 11.41 and 11.54 \AA are dominated by unidentified lines. A broad feature near 8.7 \AA is consistent with the Fe XXII excitations to the $2s2p4d^2 P_{1/2}$ and $2^2 D_{3/2}$ levels, again under the assumption that the 11.77 \AA line is unsaturated.

The analysis above strongly argues that the best description of the spectrum and most physically plausible scenario is that the density sensitive Fe XXII lines are optically thin and that the covering factor along the line of sight is near to unity. Interpreting the 11.77 \AA line as heavily saturated is inconsistent with the data. As a result, the thermal driving models presented by Netzer (2006) use a density that is too low by a factor of

approximately 5–10.

4.5. Direct Photoionization Modeling

The photoionization models presented in Paper I (and Netzer 2006) were matched to the equivalent widths of the absorption lines, but they did not employ direct spectral fitting. This is a standard procedure for the application of photoionization codes to observations of a modest number of absorption lines. It has the advantage that the user can focus on what he or she considers to be the key absorption lines, ignoring lines that provide only redundant information, and it makes it possible to take their assumptions about uncertainties in atomic rates into account. (It also forces the user to understand which features of the data the models are trying to match in achieving a best fit.) Among the disadvantages of this procedure are that it can be slow and subjective, and that it makes error estimation difficult.

More robust estimates of line parameters and saturation in X-ray spectra require proper direct spectral fitting. Spectrometers like the HETGS scatter light and can have broad line response functions, so lines that appear not to be saturated might actually be black. For instance, Figures 5 and 6 show fits to the Fe K band with XSTAR and CLOUDY (more details are given below). The Fe XXV and XXVI lines at 1.8510(4) and 1.7714(5)Å do not appear to be black. The best fit Cloudy model for the Fe K band is reproduced in Figure 7 *prior* to convolving the model with the HETGS response function. Clearly, the Fe XXV and Fe XXVI lines are actually black. This is important because it means that partial covering is not required by the data.

XSTAR (Kallman & Bautista 2001) and Cloudy (Ferland et al. 1998) are the best known, best tested and best documented general purpose photoionization codes presently available. In addition to generating new models using our own code, we have also generated a number of models using XSTAR and CLOUDY. This step is taken to add context, to test the results presented in Paper I, and to assess how model-dependent any particular results may be. Importantly, new functionality has been added to both XSTAR and Cloudy that allows grids of models to be generated and implemented into XSPEC and ISIS for direct spectral fitting. This functionality makes it possible to obtain the best possible constraints, and to obtain errors through direct comparison to data and minimization of the χ^2 goodness-of-fit statistic.

The code used in Paper I, XSTAR, and Cloudy differ from each other in minor ways, but all meet the Lexington benchmarks (Ferland 1995). Unlike the crude line-by-line fits made above, all three of these models describe lines using Voigt profiles rather than Gaussians. Voigt profiles can be especially important when lines are saturated, so their use is critical in modeling the wind observed in GRO J1655–40. There are other minor differences between the codes, including the elements and lines present in each code, but a full review of each code is beyond the scope of this paper.

Each of the XSTAR and Cloudy models described in this work were generated using a modified version of our best-fit continuum spectrum as the input flux. In order to prevent an arbitrarily high flux at low energy, the power-law component was truncated below 1 keV. This is a reasonable step as the power-law component likely arises through Comptonization. We generated sets of models based partially on the density constraints given above and the parameters in Paper I. These models all have a few properties in common: a constant density profile

($n \propto r^0$), a density of $n = 10^{14.0} \text{ cm}^{-3}$, a turbulent velocity of 300 km/s, and a line-of-sight covering factor of unity. These models generally assumed the abundances used in Paper I. The XSTAR tables generated were two-dimensional grids in ionization parameter and column density, making these variables the parameters constrained directly by fitting. Radii from XSTAR modeling were derived using the relation $\xi = L_X/nr^2$. For complementarity and to get a direct measure of inner radius, the Cloudy tables were generated as two-dimensional grids in radius and column density. These parameters were constrained by fitting, then, and the ionization parameter was derived using the prior relation.

In order to assess whether or not magnetic processes drive the wind in GRO J1655–40, it is necessary to have a point of reference. The independent models developed in Netzer (2006) are consistent with thermal driving. For the purposes of comparing our best-fit models to a thermal wind prescription, then, we also created XSTAR and Cloudy models based on the wind parameters detailed in Netzer (2006). Special care was taken to match the thermal models in detail. Whereas XSTAR version “ln” was used to generate other models, we used a modified XSTAR version “kn” that assumes an r^{-2} density profile to replicate the thermal models. This version of XSTAR has a bug in its treatment of Ni. As a result, all models generated using XSTAR version “kn” were set to have a Ni abundance of zero. The radial density profile of absorbing gas can be set directly in Cloudy, and so the same version of Cloudy was used to generate all models. All models assumed a volume filling factor of $\Omega/4\pi = 0.2$ as per Paper I, Netzer (2006), and the brief discussion above. Netzer (2006) actually describes two models with parameters that differ only minimally. We adopted a single set of parameters that accurately represent the fundamentals of both models: $\log(\xi) = 3.0$, $\log(r_0) = 10.75 \text{ cm}$, $\log(N) = 23.75$, $v_{\text{turb}} = 300 \text{ km/s}$, $\log(n_0) = 13.0$, $n(r) \propto r^{-2}$, a line of sight covering factor of 0.75, and solar abundances for all elements apart from Ca and Fe which were given twice solar abundances.

All of the photoionization models were fit to the data using ISIS as multiplicative table models modifying a disk blackbody plus power-law continuum. The neutral column density and power-law index were fixed in such fits, but all other parameters were allowed to vary. In one sense, this methodology is artificially lax, since the photoionization models were generated using the best-fit continuum model. Presumably, the best-fit continuum model could be enforced. A more pragmatic concern, though, is to assess how well the lines are fit rather than how well a fiducial continuum can cope with calibration uncertainties in specific wavelength bands. For this purpose, allowing the continuum parameters to vary is the only logical choice. A wavelength shift parameter is a part of all models. It is clear from Table 1 and Table 2 that there is a wide range in velocity shifts; therefore, this parameter was also allowed to vary in all fits.

In order to best evaluate the characteristics of the wind, we adopted three families of fits aimed at removing any possible biases associated with wavelength and/or charge state:

- One set of fits was made to the Fe K band in the 1.3–2.5Å range in order to focus on He-like Fe XXV and H-like Fe XXVI. These transitions survive even in extremely high ionization regimes, and may therefore give the best information on the innermost radial extent of the wind.
- A second set of fits were made to the 1.3–13.3Å band. The

long wavelength limit was set by the cut-off in the HEG spectra, and to avoid errors related to minor differences between the HEG and MEG spectrometers. This set of fits is meant to assess the “average” properties of the wind, and to determine which model best describes the spectrum as a whole.

- A final set of fits was made to narrow 2\AA slices between 1.3 and 13.3\AA in order to assess whether the wind changes considerably with wavelength. In essence, these fits test the possibility that one (perhaps extreme) set of parameters is needed to describe a small segment of the data, while other (perhaps less extreme) parameters are sufficient to describe the bulk of the observed absorption.

Table 3 summarizes the results of fits to the Fe K region. Models 1A and 2A are the fiducial thermal driving models based on the parameters reported by Netzer (2006). Models 1B and 2B assume an inner detection radius equal to $0.01 \times R_C$ ($10^{9.7}$ cm) – 10 times smaller than the radius at which thermal winds are possible. These models are vast statistical improvements over models 1A and 2A. Models 1C and 2C are the best-fit models for the Fe K band. The inner radius was allowed to float freely in these models; the fact that these models are 7σ and 6σ improvements over 1B and 2B, respectively, likely signals that radii significantly less than even $0.01 \times R_C$ are statistically required. Figures 5 and 6 compare the fiducial thermal models to the best-fit models.

Clearly, even the “best-fit” models are not perfect descriptions of the 1.3 – 2.5\AA spectrum. For instance, XSTAR does not include data for lines from Mn, Cr, and Ti, and so these lines are not matched by the models in Figure 5. However, the overall fit is very good, and the fact that models with a smaller inner wind radius and higher density give superior fits is common to both XSTAR and Cloudy. The high ionization parameters measured ensure an Fe XXV/XXVI line ratio that matches the data better than the fiducial thermal models. In those models, the low ionization parameter resulting from a low density and large radius creates a large Fe XXV/XXVI line ratio that fails to match the data.

Table 4 summarizes the results of fits to the broad 1.3 – 13.3\AA band. As with the fits made to the narrow Fe K band, the fiducial thermal-driving models over-predict the strength of many lines, and predict a number of lines that are not seen. Models consistent with an inner radius of $0.01 \times R_C$ (models 3B and 4B) provide vastly improved fits to the spectrum. Models 3C and 4C are the best-fit XSTAR and Cloudy models; they represent improvements over the fiducial thermal-driving models at vastly more than the 8σ level of confidence, again signaling that even smaller radii and higher ionization parameters are statistically required. The fiducial thermal models and best-fit models are compared in Figures 8 and 9.

Examination of these figures shows that the best-fit models for the 1.3 – 13.3\AA band fail to fit some lines. Indeed, there are lines that are not fit, or are fit poorly, by all of the models considered. In particular, the complex 6 – 7\AA range is not fit well; it is possible that increasing the abundance of Mg may provide a slightly better fit. Despite these difficulties, models with a small inner wind radius, high ionization parameter, and high density provide the best overall description of the data. Our fiducial thermal models appear to not only fail to describe the Fe K band, but the broad-band spectrum as well. Netzer (2006) only reported on models for the 1.3 – 9.0\AA range; when models based on the same parameters are extrapolated to 13.3\AA , many

strong absorption lines are predicted that could begin to obscure the continuum. Again, all the above findings are common to models generated with both XSTAR and Cloudy.

Finally, we made independent fits to six wavelength slices in the 1.3 – 13.3\AA range to see if our fiducial thermal-driving model is a better description of the data in any specific portion of the spectrum. Figures 10, 11, 12, and 13 show the results of fitting these models to the data. The panels in each of these figures include the relevant parameters to facilitate direct slice-by-slice comparisons. The XSTAR implementation of the fiducial thermal-driving models is shown in Figure 10, and the best-fit XSTAR model is shown in Figure 11. The Cloudy implementation of the fiducial thermal-driving models are shown in Figure 12, and the best-fit Cloudy models are depicted in Figure 13. In each slice, models with a small inner radius and high density provide vastly better fits to the data. This is true both in a statistical sense, and from visual inspection. These results are common to models generated with both XSTAR and Cloudy. The best fit model for each slice gives an inner wind radius equal to or significantly within $0.01 \times R_C$.

The XSTAR model for the 11.3 – 13.3\AA slice showing in Figure 11 provides the best overall fit to the density-sensitive Fe XXII lines at 11.77 and 11.92\AA . Note that this model also fits the putative Fe XXII line at 11.47\AA very well. The model generated using Cloudy appears to give two lines with approximately the right strength, but the wavelengths look to be slightly in error. (The nearby Ne IX 1s-2p line is over-predicted, possibly signaling that an overabundance of 2.0 was too high.) In contrast, even though the assumed partial covering acts to reduce the depth of lines relative to the continuum, the models based on Netzer (2006) predict lines that are far too strong to match the data. The XSTAR models for the Fe XXII lines are shown in detail in Figure 14.

In the exercises detailed above, the models consistent with thermal driving sometimes appear to fail partially due to a poor continuum fit. The poor continuum fits are caused by the extremely strong lines predicted by the self-consistent modeling procedure. In fact, in all cases the continuum parameters (apart from the power-law index) were allowed to float in order to allow the best possible fit. A procedure that enforced a continuum more consistent with the best broad-band continuum would cause models consistent with thermal driving to return even worse fits to the data.

Folding together the results of the three fitting exercises: models generated with XSTAR and Cloudy independently confirm that a high density ($n \leq 10^{14.0}\text{ cm}^{-3}$), highly ionized ($10^{4.5} \leq \xi \leq 10^{5.4}$) wind detected close to the black hole (10^9 – $10^{9.4}$ cm) provide a vastly superior description of the disk wind spectrum than models suggesting that the wind originates at a larger radius consistent with thermal driving. The latter models require a low ionization parameter and large radius, and therefore predict line strengths and ratios that fail to match the data.

5. DISCUSSION

The sections above detail our efforts to analyze the disk wind absorption spectrum in GRO J1655–40. Both simple phenomenological and self-consistent photoionization modeling was performed. Fits were made to specific wavelength regions, to the broadband spectrum, and in short incremental wavelength slices. Below, we begin by summarizing the properties of the wind based on our fits, and then discuss the nature of the wind.

Density: From simple Gaussian modeling of the density-sensitive Fe XXII lines, and from Monte Carlo simulations with CHIANTI, it is clear that the density of the wind is at least $10^{13.6}–10^{13.8} \text{ cm}^{-3}$. This range is significantly higher than the value of $n = 10^{13.0} \text{ cm}^{-3}$ assumed in Netzer (2006). As discussed above, this higher range is effectively a lower limit, and fits with models assuming a density of 10^{14} cm^{-3} yield excellent fits. It is clear from Figures 10–14 that a high density and high ionization are needed to match the Fe XXII lines.

Radius: All of the fits we obtained through direct fitting of the self-consistent photoionization models – regardless of the wavelength region, and regardless of the code – point to an inner wind detection radius of $r_0 \simeq 10^{9.0}–10^{9.4} \text{ cm}$. BMS and Woods et al. (1996) suggest that thermally driven winds are possible for $r_0 \geq 0.1–0.2 R_C$; in the case of GRO J1655–40, $0.1 \times R_C \simeq 10^{10.7} \text{ cm}$. Our fits clearly show that an inner detection radius of $10^{9.7} \text{ cm}$, or $0.01 \times R_C$, provides a much better description of the data, in both a statistical and visual sense. Indeed, radii significantly less than $10^{9.7} \text{ cm}$ are statistically required. An inner detection radius of $10^{9.0}–10^{9.4} \text{ cm}$ is 20–50 times smaller than the radius at which BMS and Woods et al. (1996) suggest a thermal wind can be driven. These radii correspond to $500–1250 R_{Schw}$ for GRO J1655–40. The wind may originate at a much smaller radius, but the correspondingly higher ionization parameter would prevent detection of the wind in that regime.

Thickness: The radial thickness of the wind can be estimated via the relation $\Delta(r) = N_H/n$. Models 1C, 2C, 3C, and 4C in Tables 3 and 4 then yield thicknesses of $1–5 \times 10^9 \text{ cm}$. Whereas we might trust Models 1C and 2C to give more accurate estimates of the inner detection radius r_0 , the broadband fits made with models 3C and 4C may give a better measure of thickness, so $5 \times 10^9 \text{ cm}$ is likely the best value. Thus, the thickness of the wind is at least a few times the distance between the central engine and the inner detection radius r_0 . The depth may be larger if the wind originates within the radius at which detection becomes possible. If we were to instead insist that the wind fills all of the interior radial distance with an r^{-2} density law, then $\xi = L_X/N_{HR}$ gives the radial thickness of the wind; values of $1–6 \times 10^9 \text{ cm}$ are obtained.

Mass Flux: The mass flux predicted by the thermal wind models is far lower than observed, even if the gas were beyond $0.1 R_C$ (see below). Equation 4.8 of Woods et al. (1996), or their Figure 16 scaled from a $10^8 M_\odot$ black hole to a $7 M_\odot$ black hole, predict the peak mass loss rate per unit area. For an ionizing spectrum that gives a Compton temperature close to that found in our models or Netzer’s, the maximum is $6 \times 10^{-6} \text{ g cm}^{-2} \text{ s}^{-1}$, compared to and observed mass flux of about $10^{-2} \text{ g cm}^{-2} \text{ s}^{-1}$. In terms of densities, the peak mass flux predicted by the model divided by the 500 km s^{-1} flow speed along the line of sight gives a density of $6 \times 10^{10} \text{ cm}^{-3}$. Woods et al. find that the flow is nearly vertical between $0.1 R_C$ and R_C , and the high inclination angle means that the actual speed is considerably larger than the line-of-sight component, so the predicted density is still smaller. Therefore, the thermally driven models predict densities and mass fluxes three orders of magnitude smaller than required by the observed wind spectrum.

In terms of total mass outflow rate, the best-fit values for density, inner detection radius, and thickness give a value of $3–6 \times 10^{17} \text{ g/s}$. Here again, this estimate should be regarded as a lower limit, because the velocity into our line of sight may be a small fraction of the velocity perpendicular to the disk and the wind may originate at a smaller radius. Assuming that accretion onto GRO J1655–40 has an efficiency of 10%, the mass accretion rate through the disk is approximately $5.6 \times 10^{18} \text{ g/s}$. The mass flux in the wind is at least 5–10% of that being accreted, and could easily be comparable to the mass accretion rate through the disk.

Kinetic Energy Flux: The numbers above give a kinetic energy flux of $0.5–1.0 \times 10^{13} \text{ erg cm}^{-2} \text{ s}^{-1}$. An angle of 9° above the disk midplane (see above) translates into a height of $Z = 0.16r$. For an average wind detection radius of $r_{avg} = 2 \times 10^9 \text{ cm}$, the energy flux required to lift the gas to that height is $3–6 \times 10^{14} \text{ erg cm}^{-2} \text{ s}^{-1}$. As the wind can originate at a radius smaller than the detection radius, the kinetic energy flux could also be larger than the simple estimate given here. For comparison, the viscous energy flux dissipated is given by $3GM_{BH}\dot{m}_{acc}/8\pi r^3 = 8.0 \times 10^{16} \text{ erg cm}^{-2} \text{ s}^{-1}$.

In the analysis above, three independent photoionization codes and a number of unbiased fitting experiments agree: the wind observed in GRO J1655–40 originates at least an order of magnitude (and probably more than 20–50 times closer) to the black hole than is predicted by thermal driving models, and is three orders of magnitude denser than predicted by thermal driving models. It is possible that the seminal works on Compton-heated winds in accreting systems can be revised, but it is unlikely that the full extent of these disparities can be easily overcome. Given that radiative driving also fails, the only realistic possibility remaining is that the disk wind in GRO J1655–40 is driven in part by magnetic processes.

A brief exploration of the reasons why models consistent with thermal driving might have previously appeared favorable is now in order. The analysis presented by Netzer (2006) broadly agreed with many of the conclusions of Paper I regarding elemental abundances, the inadequacy of radiation pressure driving, and the limited solid angle of the absorbing gas as seen from the black hole. But whereas Netzer (2006) minimized χ^2 for a large number of absorption lines, Paper I demanded that the model match the lowest and highest charge states of Fe, placing a more stringent limit on the ionization parameter. The latter procedure may be better for determining the innermost extent of the wind. More importantly, Netzer (2006) argued for saturation of one member of the density-sensitive line pair of Fe XXII lines, permitting a smaller density. As shown above, the Fe XXII lines are not saturated, and a higher density is required. Assuming a line-of-sight covering factor less than unity diminished the depth of lines relative to the continuum models, perhaps slightly improving the way that a combination of low density, low ionization, and large radius fit the data. In fact, the data likely rule out partial covering. Finally, the assumption of Gaussian line profiles may have affected Netzer’s modeling. When saturation is important (as with the Fe XXV and XXVI lines, among others), Voigt profiles are required. The photoionization model in Paper I, and the all of the models used in this work, used Voigt profiles.

Blandford & Payne (1982) have noted that if magnetic field lines are anchored in a disk, centrifugal forces will allow gas to escape along field lines. This magnetocentrifugal wind is the

kind found in FU Ori stars, so there is an observational confirmation of this mechanism. Tangential velocities are not encoded into X-ray absorption lines, so it is difficult to reveal clear signatures of rotation. However, geometric considerations may make it possible to discern whether this mechanism, or another magnetic mechanism, is driving a wind. The optimal configuration for powering winds in this way is one where field lines rise off the plane of the disk at an angle of about 60° (Spruit 1996). If ionized X-ray winds in X-ray binaries are primarily magnetocentrifugal, strong wind signatures should be seen for a wide range of binary inclinations.

Another possibility is that the Poynting flux generated from the magnetic viscosity thought to drive accretion through a disk can power a wind. Recent work has shown that the magnetorotational-instability (MRI) can drive turbulence, viscosity, and accretion through disks (see, e.g., Balbus & Hawley 1991; Hawley, Gammie, & Balbus 1995; Balbus & Hawley 1998; Krolik, Hawley, & Hirose 2005). Indeed, the original α -disk prescription written down by Shakura & Sunyaev (1973) envisaged a source of internal magnetic viscosity like MRI. Disk simulations incorporating MRI show that this mechanism can transmit 25% of the magnetic energy flux out of the disk to power a wind (Miller & Stone 2000), though Blaes (2007) finds much smaller values. In the case of GRO J1655–40, even the more conservative estimate of the magnetic energy flux is more than adequate to drive the observed wind to infinity, even if the true outflow rate is much larger because the flow is more nearly perpendicular to the face of the disk.

It is important to note that at the radii suggested by photoionization modeling, the blue-shifts observed in GRO J1655–40 are about an order of magnitude below the local escape velocity. X-ray absorption in black holes is only sensitive to velocities along our line of sight to the central engine. The wind may retain some of the circular motion of the disk, but this cannot be detected in absorption. Similarly, there is also good reason to think that the wind may be launched vertically from the disk; the velocity we measure along our line of sight would then be a small fraction of the total. As noted above, simulations suggest that MRI viscosity can supply the magnetic energy flux needed to drive the wind to infinity in this circumstance. The lack of emission lines from material at greater heights above the disk would naturally be explained by acceleration causing a drop in density and an increase in the ionization parameter. Thus, the data are consistent with the wind escaping to infinity, and this appears to be the most likely scenario. Even if the wind does not escape the system, but is instead a local flow stemming from a turbulent magnetic region above the disk, the implications for disk accretion onto black holes are just as interesting.

Perhaps the most detailed picture of winds driven by pressure from internal magnetic viscosity is given by Proga (2003). This work predicts that magnetic winds are likely to be dense along the plane of the disk, and to have low outflow velocities. The observed properties of the wind in GRO J1655–40 match these general predictions very well. Whereas the field lines in magnetocentrifugal winds are largely poloidal, the field lines are predominantly toroidal in this case, and the gradient in the toroidal field supplies pressure.

It is not possible to clearly distinguish which magnetic mechanism is driving the wind in GRO J1655–40, but the data and current models would seem to favor MRI pressure. The wind may not lie exclusively along the plane of the disk, but its ionization parameter will increase with any fall-off in density well

above the disk, making it difficult or impossible to detect. The dense, observable part of the wind, at least, is constrained to lie along the plane of the disk. The low outflow velocity is also in keeping with predictions. Proga (2003) finds that the rigid, largely poloidal field structure required for magnetocentrifugal driving is very difficult to maintain in dense winds. Recent work on magnetocentrifugal winds tailored to T Tauri stars, however, finds that such winds may persist even when mass loading is high and the toroidal component of the field dominates (Anderson et al. 2005).

Some additional insights into this question might be gleaned by briefly examining winds in other stellar-mass black holes. GX 339–4 is likely viewed more closely to face-on than GRO J1655–40, and the wind observed in that source is less dense than in GRO J1655–40, it has a much lower ionization parameter, and lower mass outflow rate (Miller et al. 2004). GRS 1915+105 is seen at a high inclination, like GRO J1655–40, and a highly ionized wind is seen in this source (Lee et al. 2002). The black hole candidates H1743–322 and 4U 1630–472 do not have inclinations constrained through optical or IR observations, but dipping behavior in these sources demands a high inclination in both cases. In H 1743–322, a highly ionized wind has also been observed; photoionization modeling suggests an inner launching radius of $r_0 = 1 \times 10^8$ cm (Miller et al. 2006). Recent observations of 4U 1630–472 have also revealed a highly ionized wind originating close to the black hole (Kubota et al. 2007). The winds in these sources may also be driven by magnetic processes.

Disk winds in stellar-mass black holes appear to be stronger in soft disk-dominated states than in other states. GRO J1655–40 was observed with the *Chandra*/HETGS on a separate occasion during the 2005 outburst, but in a spectrally harder state. Only the Fe XXVI line is clearly detected in that observation (a full analysis will be presented in a separate paper). H 1743–322 was observed on four occasions with the *Chandra*/HETGS, and the only observation wherein Fe XXV and Fe XXVI absorption lines are *not* detected is in the one observation made in a spectrally hard state. A preliminary analysis of archival *Chandra*/HETGS observations of GRS 1915+105 again suggests that lines are strongest in soft states, and diminished in hard states. The higher ionizing flux produced by the central engine in hard states acts to drive-up the ionization parameter and reduce the number of lines, but geometric changes and/or changes in the ability of the disk to drive a wind (perhaps due to changes in the magnetic field configuration) appear to be important too (Miller et al. 2006).

If winds are truly stronger in soft states, a number of interesting possibilities and consequences arise. Jets are quenched in soft disk-dominated states (e.g., Fender 2006), but present in low-flux, spectrally hard states. It is possible that winds and jets are anti-correlated, and that the disk alternates its outflow mode. For instance, if winds are typically very dense (as in soft states), perhaps a magnetic field configuration conducive to jets (a sort of extreme Blandford & Payne scenario) is impossible. But if the wind density drops, perhaps the jet-producing configuration becomes possible.

Though GRO J1655–40 may be the best example apart from FU Ori (and perhaps T Tauri) stars, there is already evidence that winds may be driven by magnetic processes in some white dwarfs and AGN (Mauche & Raymond 2000, Kraemer et al. 2005). In black holes and neutron stars, one hallmark of such winds may be the presence of Fe XXV and Fe XXVI absorp-

tion lines. It appears difficult to produce Fe XXV and XXVI lines of comparable strength in gas with an ionization parameter below 10^3 ; a value of $\xi \simeq 10^4$ seems more common. This typically implies a region that is very close to the central engine. The principal difficulty in searching for these lines is sensitivity: source spectra and instrument effective area curves both fall rapidly through the Fe K band. Whereas few stellar-mass black holes are persistent, many neutron star binaries are persistent sources and therefore attractive targets. Unfortunately, neutron stars are fainter than black holes at the same Eddington fraction, and their spectra are softer. Thus, whether looking for ionized winds in stellar-mass sources or AGN, deep spectroscopic observations are required. For sufficiently bright sources, the *Chandra*/HETGS is the best instrument for this purpose, but for dimmer sources the combination of high collecting area and favorable CCD modes aboard *Suzaku* may offer a pragmatic way to search for ionized winds.

Time-resolved high-resolution spectroscopy of CVs has allowed observers to identify different origins for the nature of various absorption lines, and to test how winds are driven in these systems (see, e.g., Hartley, Drew, & Long 2002; Hartley et al. 2002). Longer observations which sample large fractions of a binary phase in multiple outburst states may provide an improved means of testing the nature of winds in stellar-mass black holes and neutron stars. Whereas the properties of thermal winds should depend strongly on the launching radius and illuminating flux, the velocities and column densities of lines originating in magnetic winds may relatively independent of modest changes in the central engine. Especially since many sources are transient, such observations will be difficult to schedule and execute, but the dividends for our understanding of disk accretion onto black holes and neutron stars may be well worth the effort.

6. CONCLUSIONS

We have analyzed a *Chandra*/HETGS spectrum of the stellar-mass black hole GRO J1655–40. A highly ionized accretion disk wind is revealed in great detail. Both simple considerations and advanced modeling with three independent photoionization codes suggest that radiative and thermal driving mechanisms are likely ruled out. The wind originates at least an order of magnitude too close to the black hole (and likely 20–50 times too close), and is three orders of magnitude too dense, for it to be a thermal wind of the kind described in seminal treatments. The wind is more likely powered by magnetic driving. New models for magnetic disk winds make predictions that match the data, at least qualitatively. At present, theoretical studies provide the strongest support for MRI operating in black hole disks. Observational evidence that disk accretion onto compact objects is facilitated by magnetic processes has been elusive; this observation may provide indirect observational support.

We wish to thank Harvey Tananbaum, Jean Swank, and the *Chandra* and RXTE teams for executing our TOO observations. JMM is grateful to Gary Ferland and Ryan Porter for their patient help and insights, and hospitality during a productive visit to the University of Kentucky. We thank Mitch Begelman, Roger Blandford, Ed Cackett, Nuria Calvet, Lee Hartmann, Michiel van der Klis, Jerry Orosz, Daniel Proga, Michael Rupen, Mateusz Ruszkowski, Danny Steeghs, Marta Volonteri, and Rudy Wijnands for helpful discussions. We thank the anonymous referee for helpful comments which improved the paper. JMM acknowledges funding awarded to support this research through the *Chandra* guest observer program. This work made use of the facilities and tools available through the HEASARC web page, operated by GSFC for NASA.

REFERENCES

- Anderson, J. M., Li, Z., Krasnopolsky, R., & Blandford, R. D., 2005, *ApJ*, 630, 945
- Balbus, S., & Hawley, J. F. A., 1991, *ApJ*, 376, 214
- Bardeen, J. M., & Petterson, J. A., 1975, *ApJ*, 195, L65
- Blaes, O. 2007, in *The Central engine of Active Galactic Nuclei*, ASP Conference Series 373, 75
- Blandford, R. D., & Payne, D. G., 1982, *MNRAS*, 199, 883
- Blandford, R. D., & Znajek, R. L., 1977, *MNRAS*, 179, 433
- Begelman, M. C., McKee, C. F., & Shields, G. A., 1983, *ApJ*, 271, 70
- Cackett, E., et al., 2007, *ApJ*, subm., astro-ph/0703371
- Calvet, N., Hartmann, L., & Kenyon, S., 1993, *ApJ*, 402, 623
- Cordova, F. A., & Mason, K. O., 1982, *ApJ*, 260, 716
- Diaz Trigo, M., Parmar, A. N., Miller, J. M., Kuulkers, E., & Caballero-Garcia, M. D., 2007, *A&A*, 462, 657
- Fender, R. P., 2006, in “Compact Stellar X-ray Sources”, eds. W. Lewin and M. van der Klis, Cambridge University Press, Cambridge, astro-ph/0303339
- Ferland, G., 1995, in “The Analysis of Emission Lines: A Meeting in Honor of the 70th Birthdays of D. E. Osterbrock and M. J. Seaton”, proceedings of the Space Telescope Science Institute Symposium, May 16–18 1994, eds. R. Williams and M. Livio, Cambridge University Press
- Ferland, G. T., Korista, K. T., Verner, D. A., Ferguson, J. W., Kingdon, J. B., & Verner, E. M., 1998, *PASP*, 110, 761
- Foellmi, C., Depagne, E., Dall, T. H., & Mirabel, I. F., 2006, *A&A*, 457, 249
- Hartley, L. E., Drew, J. E., & Long, K. S., 2002, *MNRAS*, 336, 808
- Hartley, L. E., Drew, J. E., Long, K. S., Knigge, C., & Proga, D., 2002, *MNRAS*, 332, 127
- Hjellming, R. M., & Rupen, M. P., 1995, *Nature*, 375, 464
- Homan, J., & Belloni, T., 2005, *Ap&SS*, 300, 107
- Homan, J., Miller, J. M., Wijnands, R., et al., 2005, *ApJ*, 623, 383
- Kallman, T., & Bautista, M., 2001, *ApJS*, 133, 221
- Kaspi, S., et al., 2002, *ApJ*, 574, 643
- van der Klis, M., 2006, in “Compact Stellar X-ray Sources”, eds. W. Lewin and M. van der Klis, Cambridge University Press, Cambridge
- Kraemer, S. B., George, I. M., Crenshaw, D. M., et al., 2005, *ApJ*, 633, 693
- Krolik, J. H., Hawley, J. F., & Hirose, S., 2005, *ApJ*, 622, 1008
- Mauche, C., Liedahl, D. A., & Fournier, K., 2003, *ApJ*, 588, L101
- Mauche, C., & Raymond, J., 2000, *ApJ*, 541, 924
- McClintock, J. E., & Remillard, R. A., 2006, in “Compact Stellar X-ray Sources”, eds. W. H. G. Lewin and M. van der Klis, Cambridge: Cambridge University press, astro-ph/0306213
- McHardy, I. M., Koerding, E., Knigge, C., Uttley, P., & Fender, R. F., 2006, *Nature*, 444, 730
- Miller, J. M., 2007, *ARA&A*, 45, 441
- Miller, J. M., Raymond, J., Fabian, A. C., et al., 2006, *Nature*, 441, 953
- Miller, J. M., Raymond, J., Homan, J., et al., 2006b, *ApJ*, 646, 394
- Miller, J. M., Raymond, J., Fabian, A. C., et al., 2004a, *ApJ*, 601, 450
- Netzer, H., 2006, *ApJ*, 652, L117
- Orosz, J., & Baily, C. D., 1997, *ApJ*, 477, 876
- Proga, D., 2003, *ApJ*, 585, 406
- Proga, D., Stone, J. M., & Drew, J. E., 1998, *MNRAS*, 295, 595
- Proga, D., Stone, J. M., & Kallman, T., 2000, *ApJ*, 585, 406
- Rykoff, E. S., Miller, J. M., Steeghs, D., & Torres, M. A. P., 2007, *ApJ*, in press
- Sala, G., Greiner, J., Vink, J., Haberl, F., Kendziorra, E., & Zhang, X. L., 2007, *A&A*, 461, 1049
- Shakura, N. I., & Sunyaev, R. A., 1973, *A&A*, 24, 337
- Spruit, H. C., 1996, in “Physical Processes in Binary Stars”, eds. R. A. M. J. Wijers, M. B. Davies, and C. A. Tout, NATO ASI series, Kluwer Dordrecht, astro-ph/9602022
- Vaughan, S., & Uttley, P., 2005, *MNRAS*, 362, 235
- Vrtilek, S., et al., 1990, *A&A*, 234, 162
- Woods, D. T., Klein, R. I., Castor, J. I., McKee, C. F., & Bell, J. B., 1996, *ApJ*, 461, 767
- Young, P. R., Del Zanna, G., Landi, E., Dere, K. P., Mason, H. E., and Landini, M., 2003, *ApJS*, 144, 135

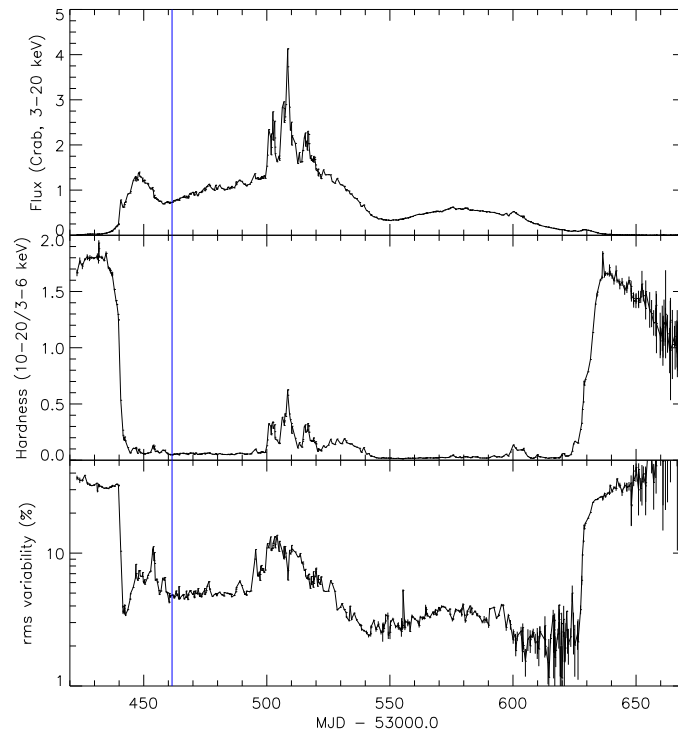


FIG. 1.— *RXTE* made numerous pointed observations of GRO J1655–40 during its 2005 outburst. Flux (in Crab units), spectral hardness, and rms variability are plotted versus time in the figure above, based on these pointed observations. The blue vertical line in each panel shows the time at which the *Chandra* observation was obtained. (Error bars are plotted, but are often very small.)

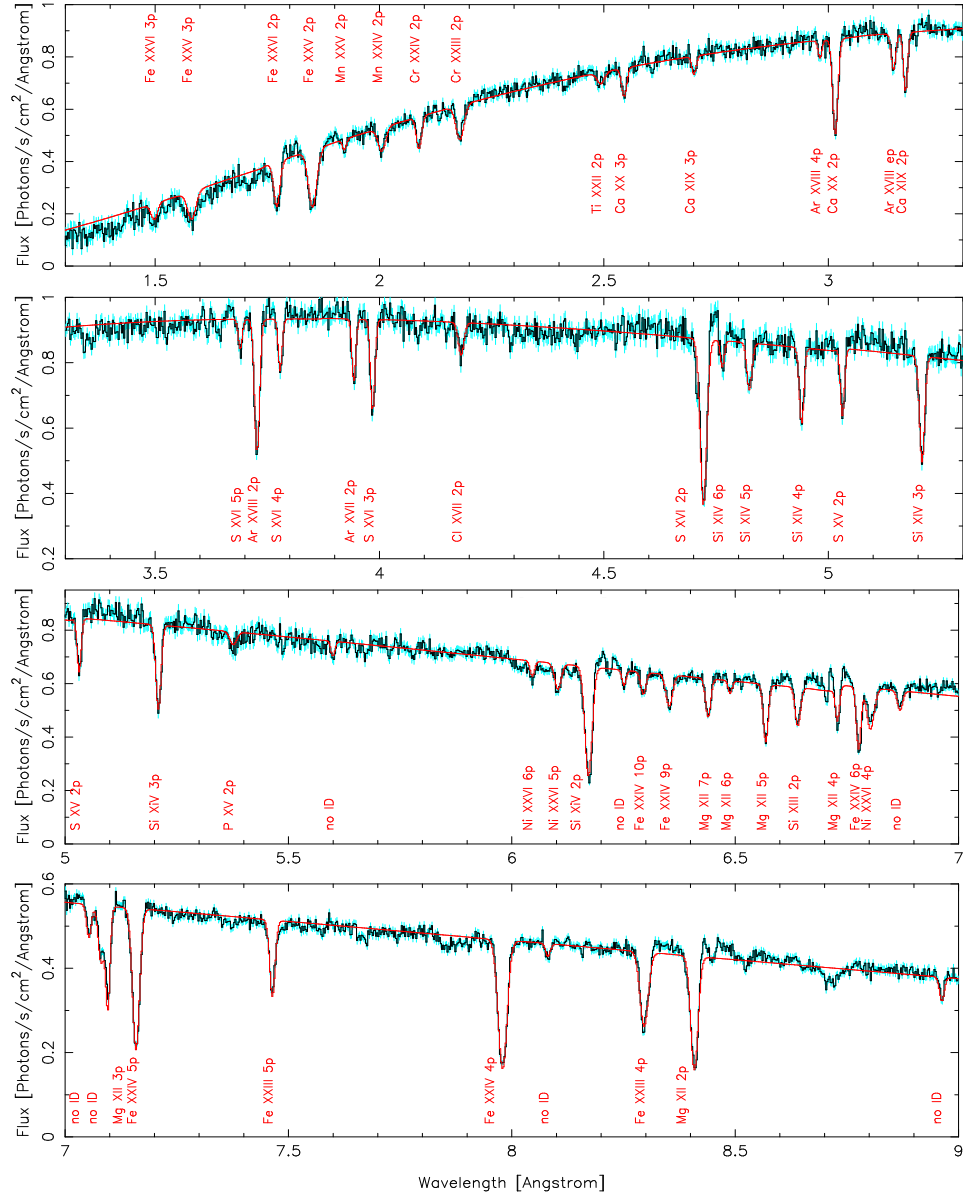


FIG. 2.— Phenomenological fits to the *Chandra*/HETGS spectrum of GRO J1655–40 are shown above. The continuum was only fit to the wavelength slice shown in each panel, and all lines were fit with simple Gaussian functions. Line identifications are given based on the strategy outlined in the text.

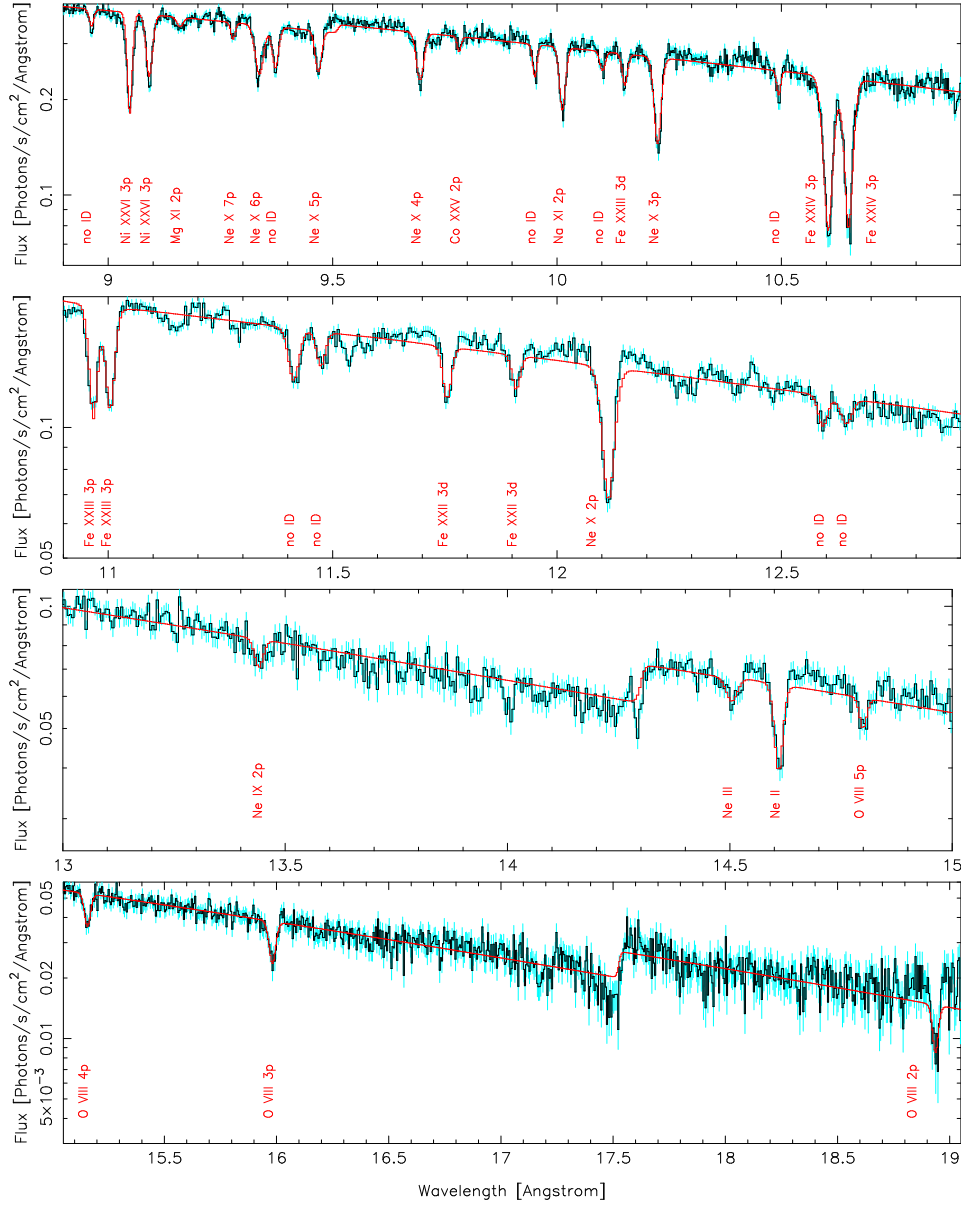


FIG. 3.— Phenomenological fits to the *Chandra*/HETGS spectrum of GRO J1655–40 are shown above. The continuum was only fit to the wavelength slice shown in each panel, and all lines were fit with simple Gaussian functions. Line identifications are given based on the strategy outlined in the text.

TABLE 1

Gaussian Line Parameters and Line Flux Limits, $Z < 17$

Ion and Transition	Meas. (Å)	Theor. (Å)	Shift (km/s)	FWHM		Flux (10^{-3} ph/cm ² /s)	W (mÅ)	N_z (10^{17} cm ⁻²)
				(10^{-3} Å)	(km/s)			
O VIII 1s–5p	14.800(2)	14.8206	420(40)	< 10	< 200	1.4(3)	23(5)	9(2)
O VIII 1s–4p	15.157(2)	15.1762	380(40)	28(5)	550(80)	4.0(4)	77(8)	13(1)
O VIII 1s–3p	15.982(2)	15.987	90(30)	31(5)	580(90)	5.1(5)	120(10)	7.5(8)
O VIII 1s–2p	18.938(2)	18.9689	480(40)	24(5)	380(80)	1.2(2)	80(8)	0.7(1)
Ne X 1s–7p	9.2786(6)	9.2912	410(20)	5(2)	200(100)	1.3(2)	3.6(7)	10(2)
Ne X 1s–6p	9.3365(6)	9.3616	800(20)	22(1)	700(40)	6.6(3)	22(1)	35(1)
Ne X 1s–5p	9.4685(4)	9.4807	390(20)	14(1)	440(30)	4.1(3)	12(1)	11(1)
Ne X 1s–4p	9.6949(5)	9.7082	410(10)	18(2)	560(50)	5.5(3)	16(1)	6.6(3)
Ne X 1s–3p	10.2246(3)	10.2389	420(10)	17(1)	500(30)	8.3(2)	30(7)	4.1(1)
Ne X 1s–2p	12.1152(5)	12.1330	550(10)	29(1)	720(20)	8.2(4)	57(3)	1.05(5)
Ne IX 1s ² –1s2p	13.441(4)	13.4471	140(80)	14	300	1.8(4)	22(5)	0.20(5)
Ne III	14.504(3)	14.526	450(50)	20(10)	400(200)	1.5(2)	22(3)	1.1(2)
Ne II	14.611(1)	14.631	410(20)	14(2)	300(30)	3.8(3)	58(5)	4.9(4)
Na XI 1s–2p	10.0122(3)	10.0250	380(10)	13.2(5)	400(20)	5.6(2)	18.7(7)	0.51(2)
Mg XII 1s–7p	6.4395(3)	6.4486	420(10)	9(1)	420(50)	3.2(1)	5.1(2)	28(1)
Mg XII 1s–6p	6.4888(5)	6.4974	400(20)	< 6	< 300	0.8(1)	1.3(2)	4.4(6)
Mg XII 1s–5p	6.5685(2)	6.5801	530(10)	8.0(5)	360(30)	4.7(1)	7.7(2)	14.4(4)
Mg XII 1s–4p	6.7275(3)	6.7379	460(10)	< 6	< 300	2.5(1)	4.2(2)	3.6(2)
Mg XII 1s–3p	7.0969(4)	7.1062	390(20)	5.4(5)	230(20)	3.9(3)	9.8(9)	2.8(3)
Mg XII 1s–2p	8.4087(2)	8.4210	440(10)	16.7(3)	590(10)	9.6(1)	22.6(2)	0.87(1)
Mg XI 1s ² –1s2p	9.159(2)	9.1688	320(70)	13	400	1.0(1)	2.7(3)	0.049(5)
Si XIV 1s–6p	4.764(2)	4.7704	400(100)	< 5.0	< 300	1.0(1)	1.2(1)	7.5(8)
Si XIV 1s–5p	4.8243(7)	4.8311	420(40)	9(2)	600(100)	2.4(2)	2.8(2)	9.7(9)
Si XIV 1s–4p	4.9407(3)	4.9469	380(20)	6(1)	360(60)	3.6(2)	4.2(2)	6.7(3)
Si XIV 1s–3p	5.2090(3)	5.2172	470(20)	9.7(7)	560(40)	5.9(2)	7.2(2)	3.8(1)
Si XIV 1s–2p	6.1721(1)	6.1822	490(10)	15.5(2)	750(10)	11.9(1)	18.5(2)	1.32(1)
Si XIII 1s ² –1s2p	6.6402(2)	6.6480	350(10)	10(1)	450(50)	3.4(1)	5.7(1)	0.19(1)
P XV 1s–2p	5.375(2)	5.383	700(200)	–	400	1.0(2)	1.3(3)	0.12(3)
S XVI 1s–5p	3.690(1)	3.6959	480(80)	< 5	< 400	1.1(2)	1.2(2)	7(1)
S XVI 1s–4p	3.780(1)	3.7845	360(80)	< 5	< 400	1.9(2)	2.0(2)	5.4(5)
S XVI 1s–3p	3.9858(3)	3.9912	400(30)	6(1)	450(80)	3.9(2)	4.2(2)	3.8(2)
S XVI 1s–2p	4.7221(2)	4.7292	450(10)	14.4(7)	910(50)	11.3(2)	12.8(2)	1.55(2)
S XV 1s ² –1s2p	5.0318(4)	5.0387	410(20)	< 5	< 400	2.9(2)	3.4(2)	0.20(2)

Parameters of the disk wind absorption lines observed in GRO J1655–40 for elements with $Z < 17$ are given above. For clarity, the lines are listed by element in order of ascending atomic number, and in order of increasing wavelength by element and ion. The spectral continua were fit locally using power-law models modified by neutral photoelectric absorption edges (due to the interstellar medium) where appropriate. The lines were fit with simple Gaussian models. The errors quoted above are 1σ uncertainties. Line significances were calculated by dividing line flux by its 1σ error. Where errors are not given, the parameter was fixed at the quoted value. Line widths consistent with zero are not resolved.

TABLE 2

Gaussian Line Parameters for $Z > 17$ Elements and Unidentified Lines

Ion and Transition	Meas. (Å)	Theor. (Å)	Shift (km/s)	FWHM		Flux (10^{-3} ph/cm ² /s)	W (mÅ)	N_z (10^{17} cm ⁻²)
				(10^{-3} Å)	(km/s)			
Cl XVII $1s-2p$	4.182(1)	4.187	400(100)	9(2)	600(200)	1.5(2)	1.6(2)	0.25(3)
Ar XVIII $1s-4p$	2.981(1)	2.9875	700(100)	< 5	< 500	0.8(1)	0.9(1)	3.9(5)
Ar XVIII $1s-3p$	3.1454(5)	3.1506	500(50)	6(1)	600(100)	2.0(2)	2.2(2)	3.2(3)
Ar XVIII $1s-2p$	3.7271(2)	3.7329	470(20)	8.7(7)	700(50)	6.3(2)	8.0(3)	1.6(1)
Ar XVII $1s^2-1s2p$	3.9429(4)	3.9488	450(30)	< 5	< 500	2.3(1)	2.6(1)	0.24(1)
K XIX $1s-2p$	–	3.348	–	–	800	1.0(2)	1.0(2)	0.24(5)
Ca XX $1s-3p$	2.5452(6)	2.5494	490(70)	9(2)	1100(100)	1.7(2)	2.2(2)	4.8(5)
Ca XX $1s-2p$	3.0187(2)	3.0203	160(20)	9.2(7)	910(70)	5.75(7)	6.66(8)	2.0(1)
Ca XIX $1s^2-1s3p$	2.701(1)	2.7054	500(100)	< 10	< 1100	0.9(1)	1.1(1)	1.1(1)
Ca XIX $1s^2-1s2p$	3.1722(3)	3.1772	470(30)	< 10	< 1100	2.9(2)	3.2(2)	0.46(4)
Sc XXI $1s-2p$	–	2.740	–	–	1500	< 0.1	< 0.13	< 0.05
Ti XXII $1s-2p$	2.493(2)	2.4966	430(240)	17(5)	2000(600)	1.0(2)	1.3(3)	1.7(3)
V XXIII $1s-2p$	–	2.2794	–	–	1500	< 0.7	< 0.7	< 0.4
Cr XXIV $1s-2p$	2.0880(6)	2.0901	300(80)	10(2)	1400(300)	2.0(2)	3.4(3)	6.3(6)
Cr XXIII $1s^2-1s2p$	2.1794(6)	2.1821	370(80)	19(2)	2600(300)	3.1(2)	4.8(3)	1.6(2)
Mn XXV $1s-2p$	1.922(2)	1.9247	400(300)	< 154	< 2000	0.5(1)	1.0(2)	1.1(2)
Mn XXIV $1s^2-1s2p$	2.005(1)	2.0062	200(140)	17(2)	2500(300)	2.0(2)	3.7(4)	3.7(4)
Fe XXVI $1s-3p$	1.498(2)	1.5028	1000(400)	12	2400	1.1(2)	5(1)	32(6)
Fe XXVI $1s-2p$	1.7714(5)	1.7798	1400(100)	12(1)	2400(200)	3.1(2)	7.8(5)	6.7(4)
Fe XXV $1s^2-1s3p$	1.581(1)	1.5732	1500(200)	20	3800	2.6(2)	9.7(9)	28(3)
Fe XXV $1s^2-1s2p$	1.8510(4)	1.8504	0(100)	20(1)	3800(300)	5.4(2)	12.6(5)	5.2(2)
Fe XXIV $1s^22s-1s^210p$	6.2946(5)	6.3055	–	10(1)	480(40)	1.8(2)	2.8(3)	21(1)
Fe XXIV $1s^22s-1s^29p$	6.3523(4)	6.3475	–	14(1)	660(50)	3.3(2)	5.2(3)	28(2)
Fe XXIV $1s^22s-1s^28p$	blend	–	–	–	–	–	–	–
Fe XXIV $1s^22s-1s^27p$	blend	–	–	–	–	–	–	–
Fe XXIV $1s^22s-1s^26p$	6.7773(2)	6.7870	430(10)	8.2(5)	360(20)	5.4(1)	10.2(2)	11.9(2)
Fe XXIV $1s^22s-1s^25p$	7.1590(1)	7.1690	420(10)	15.8(2)	660(10)	10.37(3)	19.3(1)	10.6(1)
Fe XXIV $1s^22s-1s^24p$	7.9795(1)	7.9893	370(10)	20.2(1)	760(10)	13.1(2)	28.2(4)	5.15(7)
Fe XXIV $1s^22s-1s^23p$	10.6043(3)	10.619	420(10)	27.3(7)	770(20)	13.7(4)	60(1)	2.30(4)
Fe XXIV $1s^22s-1s^23p$	10.6494(3)	10.663	380(10)	23.8(5)	670(20)	11.9(2)	52(1)	3.95(5)
Fe XXIII $2s^2-2s5p$	7.4639(2)	7.4722	330(10)	11.6(5)	470(20)	4.15(4)	8.2(1)	2.27(4)
Fe XXIII $2s^2-2s4p$	8.2963(2)	8.3029	240(10)	18.1(5)	650(20)	7.0(1)	16.3(2)	1.49(2)
Fe XXIII $2s^2-2p3d$	10.1512(6)	10.175	700(20)	10(2)	290(60)	2.7(2)	16(2)	5.3(7)
Fe XXIII $2s^2-2p3s$	–	10.560	–	–	–	–	–	–
Fe XXIII $2s^2-2s3p$	10.9671(3)	10.981	380(10)	16(1)	440(30)	7.0(3)	40(2)	0.54(3)
Fe XXIII $2s^2-2s3p4$	11.0049(5)	11.018	360(10)	17(1)	460(30)	6.8(3)	33(2)	1.1(1)
Fe XXII $2s^22p-2s^23d$	11.755(1)	11.770	380(20)	8(1)	200(30)	2.4(1)	16.0(6)	0.19(1)
Fe XXII $2s^22p-2s^23d$	11.909(2)	11.920	280(50)	12(2)	300(50)	1.7(1)	12.7(7)	0.17(1)
Ni XXVI $1s^22s-1s^26p$	6.045(1)	–	–	9.2(5)	450(30)	1.4(2)	2.1(3)	–
Ni XXVI $1s^22s-1s^25p$	6.103(1)	6.120	830(50)	16(2)	800(100)	2.6(2)	3.9(4)	4.2(5)
Ni XXVI $1s^22s-1s^24p$	6.8029(4)	6.8163	650(20)	27(1)	1200(50)	5.7(1)	9.5(2)	2.3(1)
Ni XXVI $1s^22s-1s^23p$	9.0479(2)	9.061	430(10)	15.1(5)	500(20)	6.6(1)	18.5(3)	1.04(1)
Ni XXVI $1s^22s-1s^23p$	9.0917(4)	9.105	440(10)	11.8(4)	400(30)	4.5(1)	12.4(3)	1.31(3)
Co XXV $1s^22s-1s^23p$	9.782(1)	9.795	400(40)	8(4)	200(100)	1.0(2)	3.2(6)	0.15(3)
no ID; Al XIII $1s-5p$?	5.600(1)	–	–	6(2)	400	0.85(15)	1.1(2)	–
no ID; Ni XXVI $2p-5d$?	6.250(1)	–	–	< 4	< 200	1.0(2)	1.5(3)	–
no ID; Ni XXVI $2p-4s$?	7.0555(8)	–	–	7(2)	300(100)	1.3(1)	2.4(2)	–
no ID; Ni XXVI $2p-4d$?	7.0815(8)	–	–	12(2)	500(100)	3.0(3)	5.4(5)	–
no ID; Ni XXVI $2p-3d$?	9.3726(4)	–	–	14(1)	450(30)	4.2(2)	12.3(6)	–
no ID; Ni XXV $2s2p-2s3d$?	9.9509(5)	–	–	6(2)	200(50)	2.3(2)	7.7(6)	–
no ID	6.8690(5)	–	–	10(2)	440(80)	1.7(1)	2.9	–
no ID	8.081(2)	–	–	7(2)	260(80)	0.6(1)	1.4	–
Fe XXII?	8.960(1)	–	–	< 5	< 200	1.0(1)	2.6	–
no ID	10.1015(6)	–	–	12(5)	400(100)	1.7(2)	5.8	–
no ID	10.494(1)	–	–	3(3)	100(100)	1.5(2)	6.2	–
no ID	11.413(2)	–	–	57(9)	1500(200)	7(1)	38.9	–
Fe XXII?	11.472(2)	–	–	12(5)	300(100)	1.6(3)	10.7	–
no ID	12.593(2)	–	–	19(7)	500(200)	2.3(4)	19.5	–
no ID	12.644(3)	–	–	24(7)	600(100)	2.1(4)	18.7	–

Parameters of the disk wind absorption lines observed in GRO J1655–40 for elements with $Z \geq 17$ are given above. For clarity, the lines are listed by element in order of ascending atomic number, and in order of increasing wavelength by element and ion. The spectral continua were fit locally using power-law models modified by neutral photoelectric absorption edges (due to the interstellar medium) where appropriate. The lines were fit with simple Gaussian models. The errors quoted above are 1σ uncertainties. Line significances were calculated by dividing line flux by its 1σ error. Where errors are not given, the parameter was fixed at the quoted value. Line widths consistent with zero are not resolved.

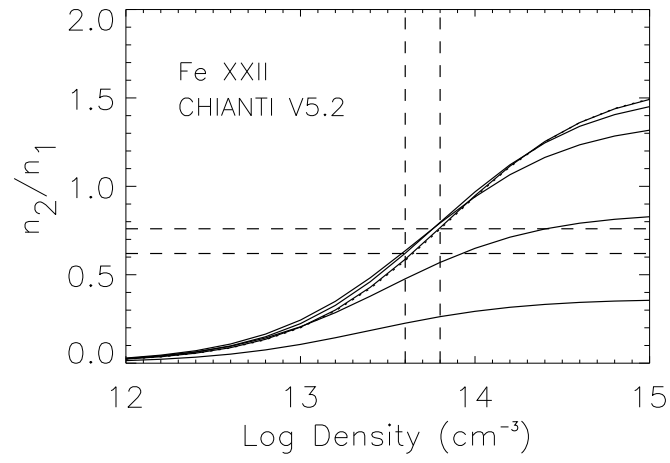


FIG. 4.— The ratio of the populations of the fine structure states of the ground level of Fe XXII predicted by CHIANTI are shown here. The curves correspond to temperatures $\log T = 5.0, 5.3, 5.7, 6.0$ and 6.3 from bottom to top along the high density edge of the plot. The two Fe XXII lines detected in GRO J1655–40 represent a density diagnostic that is as sensitive as better-known He-like triplets.

TABLE 3

Fits to the 1.3–2.5Å Fe K Band with XSTAR and Cloudy Models

Model	Code	Range	Profile	$\log(n_0)$	$\log(N_H)$	$\log(\xi)$	$\log(r_0)$	χ^2/ν	χ^2/ν
1A	XSTAR kn	1.3–2.5Å	r^{-2}	13.0	23.68	3.0	10.7	6749/516	13.1
1B	XSTAR ln	1.3–2.5Å	r^0	14.0	23.14(3)	4.2	9.7	1670/517	3.23
1C	XSTAR ln	1.3–2.5Å	r^0	14.0	23.1(1)	4.80(5)	9.44(3)	1494/516	2.88
2A	Cloudy	1.3–2.5Å	r^{-2}	13.0	23.75	3.0	10.7	2463/517	4.78
2B	Cloudy	1.3–2.5Å	r^0	14.0	23.36(1)	4.3	9.7	1232/517	2.43
2C	Cloudy	1.3–2.5Å	r^0	14.0	23.70(1)	5.7(2)	9.0(1)	1147/516	2.21

Fits to the 1.3–2.5Å Fe K band with various XSTAR and CLOUDY table models are listed above. This region probes the hottest, most ionized part of the wind, and therefore gives the best picture of the innermost extent of the wind. Models 1A and 2A were generated using the thermal wind parameters given in Netzer (2006). Models 1B and 2B assume the same density as the best-fit models (1C and 2C), but fix the radius at $r = 10^{9.7}$ cm, or $0.01 \times R_C$. Statistically, models 1B and 2B are vastly superior fits to the data than models 1A and 2A. However, the data and models are of such quality that small changes in radius can be distinguished, and indeed smaller radii are statistically required. Models 1C and 2C are the best-fit models; they are 7σ and 6σ improvements over model 1B and 2B, respectively. Models 2B and 2C have slightly enhanced abundances of four times solar for Ca, Sc, Ti, V, Cr, and Mn rather than merely twice solar as in the other models; these abundances give slightly better fits. For full details on all of these models, please see the text. Errors given in parentheses denote the error in the last significant digit, and are 1σ confidence errors. Where errors are not given, the model parameter was fixed.

TABLE 4

Broad-band fits with XSTAR and Cloudy Models

Model	Code	Range	Profile	$\log(n_0)$	$\log(N_H)$	$\log(\xi)$	$\log(r_0)$	χ^2/ν	χ^2/ν
3A	XSTAR kn	1.3–13.3Å	r^{-2}	13.0	23.68	3.0	10.7	340474/4794	71.0
3B	XSTAR ln	1.3–13.3Å	r^0	14.0	23.46(1)	4.3	9.7	47117/4793	9.83
3C	XSTAR ln	1.3–13.3Å	r^0	14.0	23.65(1)	4.88(2)	9.41(2)	43879/4792	9.16
4A	Cloudy	1.3–13.3Å	r^{-2}	13.0	23.75	3.0	10.7	212478/4794	44.26
4B	Cloudy	1.3–13.3Å	r^0	14.0	23.46(1)	4.3	9.7	87260/4793	18.20
4C	Cloudy	1.3–13.3Å	r^0	14.0	23.67(2)	4.88(2)	9.40(2)	85752/4792	17.89

Fits to the 1.3–13.3Å band with various XSTAR and CLOUDY table models are listed above. Fitting single models to this broad bandpass gives a measure of the average wind properties. Models 3A and 4A were generated using the thermal wind parameters given in Netzer (2006). Models 3B and 4B assume the density used in the best-fit models (3C and 4C), but fix the radius at $r = 10^{9.7}$ cm, or $0.01 \times R_C$. Here again, models 3B and 4B are enormous statistical improvements over models 3A and 4A, and smaller radii than those assumed in models 3B and 4B are statistically required. Models 3C and 4C are vast statistical improvements over models 3B and 4B. Models 4B and 4C have slightly enhanced abundances of four times solar for Ca, Sc, Ti, V, Cr, and Mn rather than merely twice solar as in the other models; these abundances give slightly better fits. For full details on all of these models, please see the text. Errors given in parentheses denote the error in the last significant digit, and are 1σ confidence errors. Where errors are not given, the model parameter was fixed.

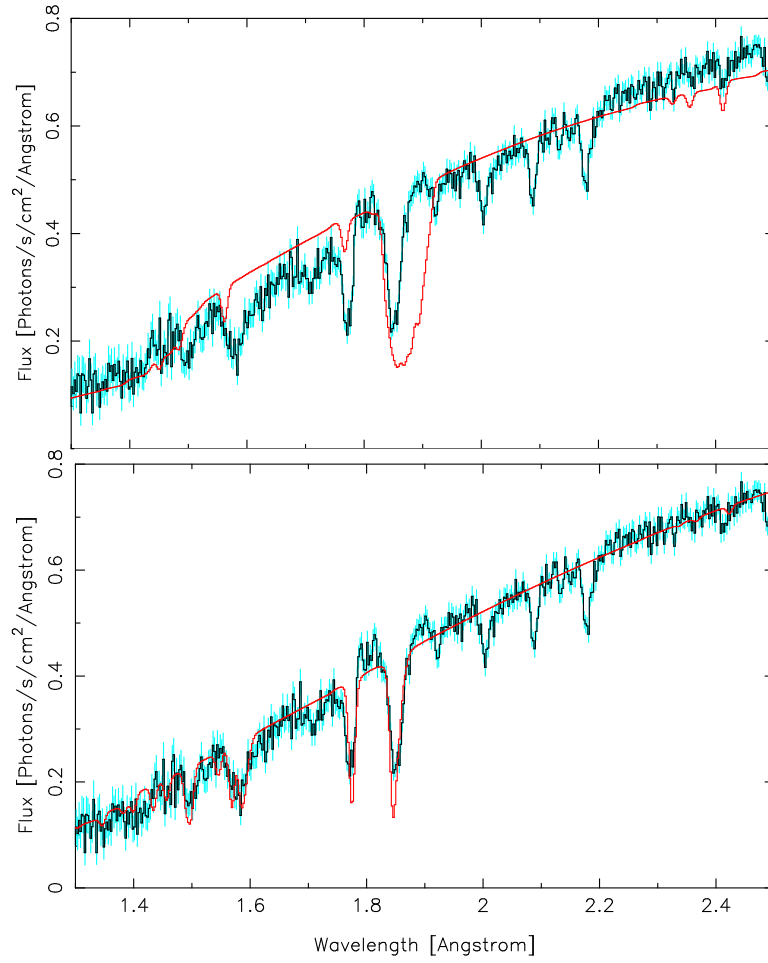


FIG. 5.— The plot above shows the crucial Fe K wavelength regime of the wind absorption spectrum, fit with XSTAR models. The He-like Fe XXV line at 1.850\AA and H-like Fe XXVI line at 1.77\AA are expected to arise in the most ionized part of the wind, and thus give the best measure of the innermost extent of the wind. Model 1A is shown in the upper panel; it is consistent with a thermally-driven wind, and is based on the models described in Netzer (2006). Model 1C is shown in the lower panel; it is the best-fit XSTAR model, and corresponds to a wind where magnetic driving is likely to be important. For more details on the models shown above, please see Table 3 and the text.

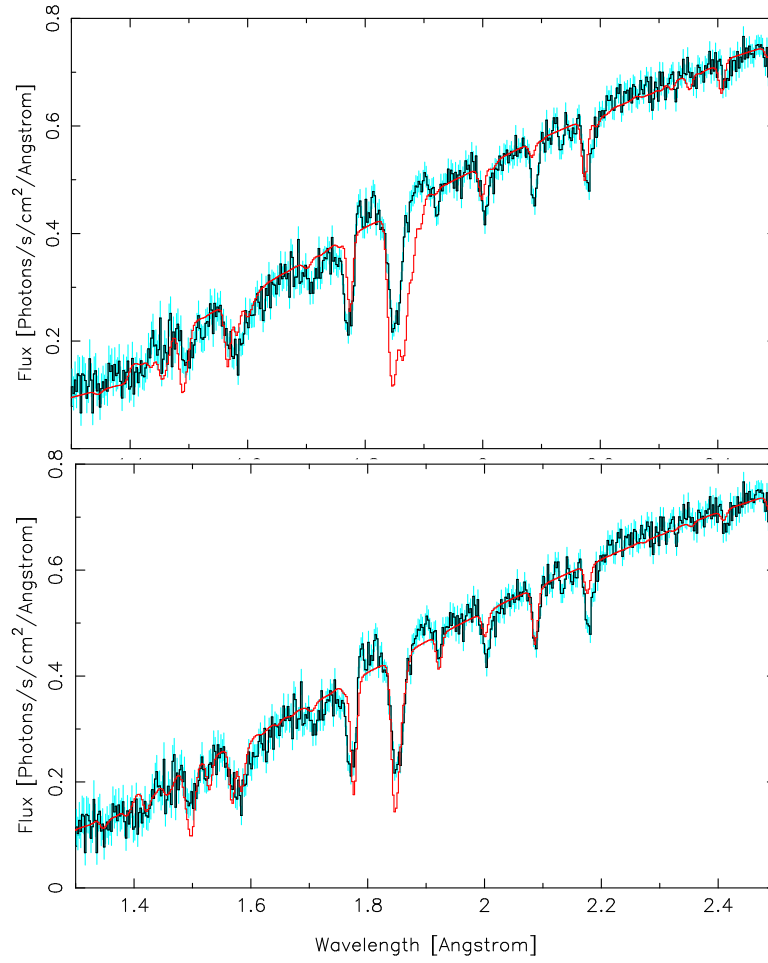


FIG. 6.— The plot above again shows the crucial Fe K wavelength regime of the wind absorption spectrum, fit with Cloudy models. The He-like Fe XXV line at 1.850\AA and H-like Fe XXVI line at 1.77\AA are expected to arise in the most ionized part of the wind, and thus give the best measure of the innermost extent of the wind. Model 2A is shown in the upper panel; it is consistent with a thermally-driven wind, and is based on the models described in Netzer (2006). Model 2C is shown in the lower panel; it is the best-fit XSTAR model, and corresponds to a wind where magnetic driving is likely to be important. For more details on the models shown above, please see Table 3 and the text.

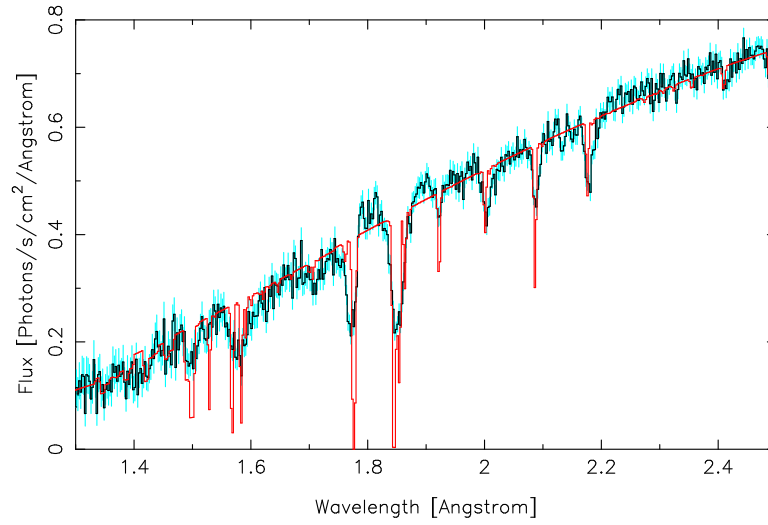


FIG. 7.— The plot above shows the crucial short wavelength regime of the rich wind absorption spectrum. The model shown above is the best-fit Cloudy model (2C), but is shown prior to convolution with the HETGS response function. The Fe XXV and Fe XXVI absorption lines at 1.850\AA and 1.77\AA are actually black at line center, though they do not appear to be black after convolving with the instrument response (see the bottom panel in Figure 6). To address issues such as saturation, direct fitting is the most robust means of modeling spectra.

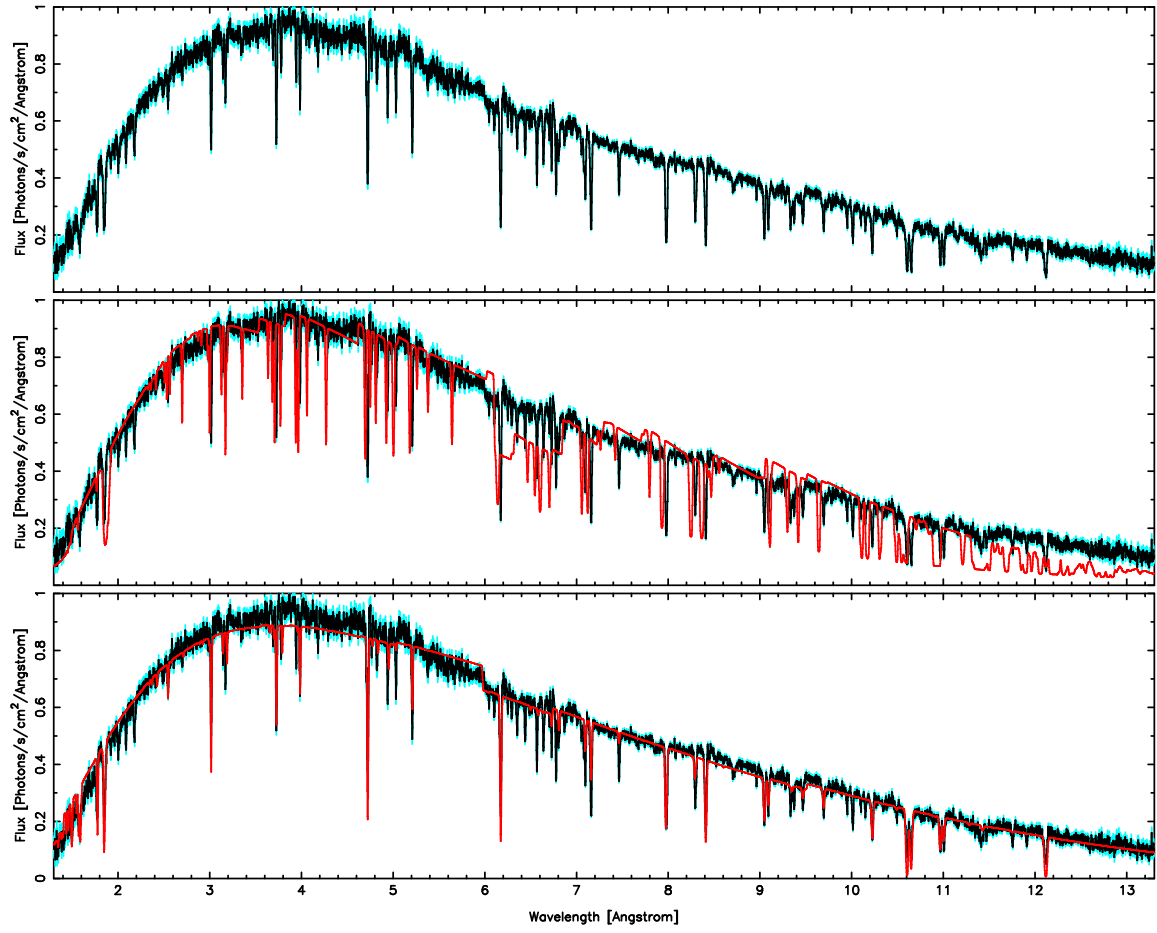


FIG. 8.— The plot above shows the 1.3–13.3 Å spectrum of GRO J1655–40. The top panel merely depicts the spectrum. The middle panel shows the spectrum fit with an XSTAR model (3A) consistent with a thermally-driven wind, based on the models described by Netzer (2006). The bottom panel shows the spectrum fit with our best-fit XSTAR model (3C), and corresponds to a scenario where magnetic driving is likely to be important. For details on the models shown above, please see Table 4 and the text.

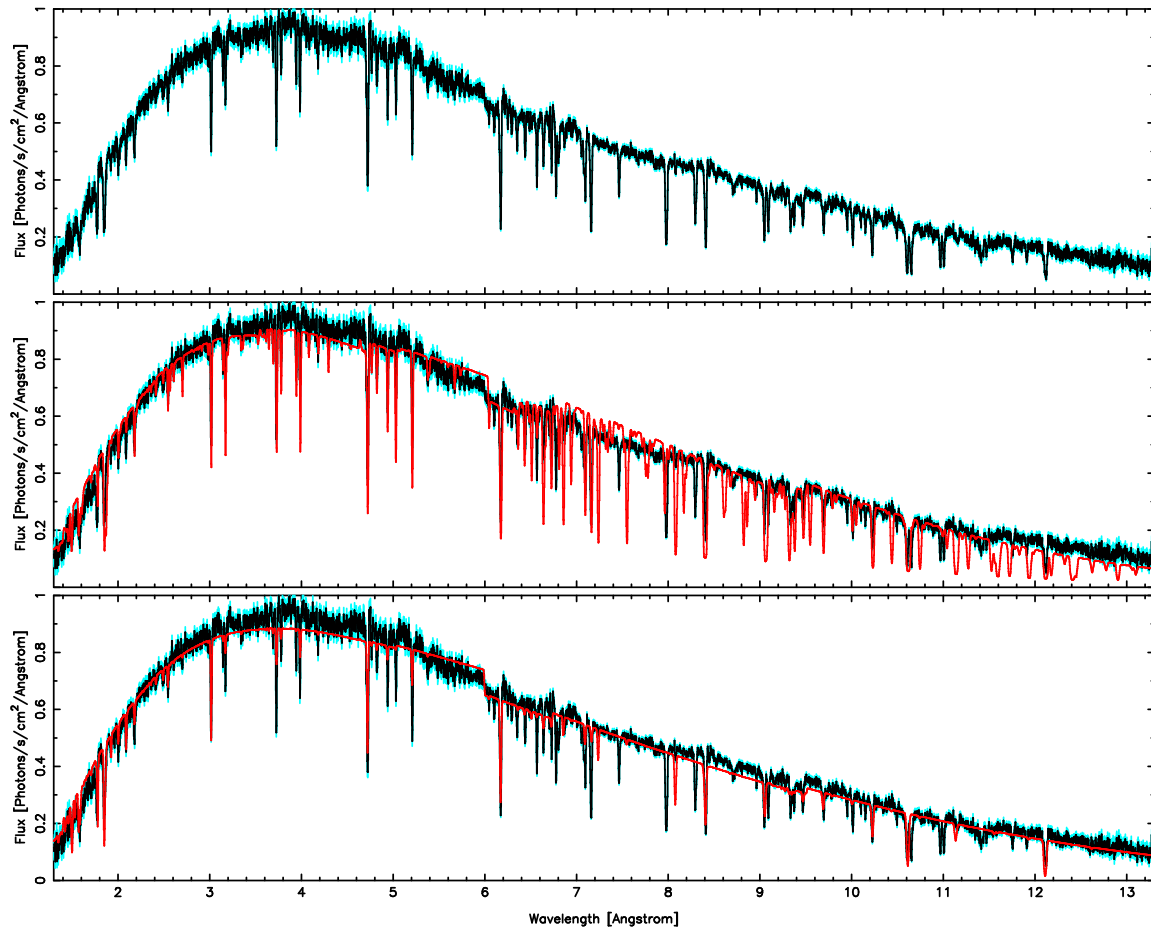


FIG. 9.— The plot above shows the 1.3–13.3Å spectrum of GRO J1655–40. The top panel merely depicts the spectrum. The middle panel shows the spectrum fit with a Cloudy model (4A) consistent with a thermally–driven wind, based on the models described by Netzer (2006). The bottom panel shows the spectrum fit with our best-fit Cloudy model, and corresponds to a scenario where magnetic driving is likely to be important. For details on the models shown above, please see Table 4 and the text.

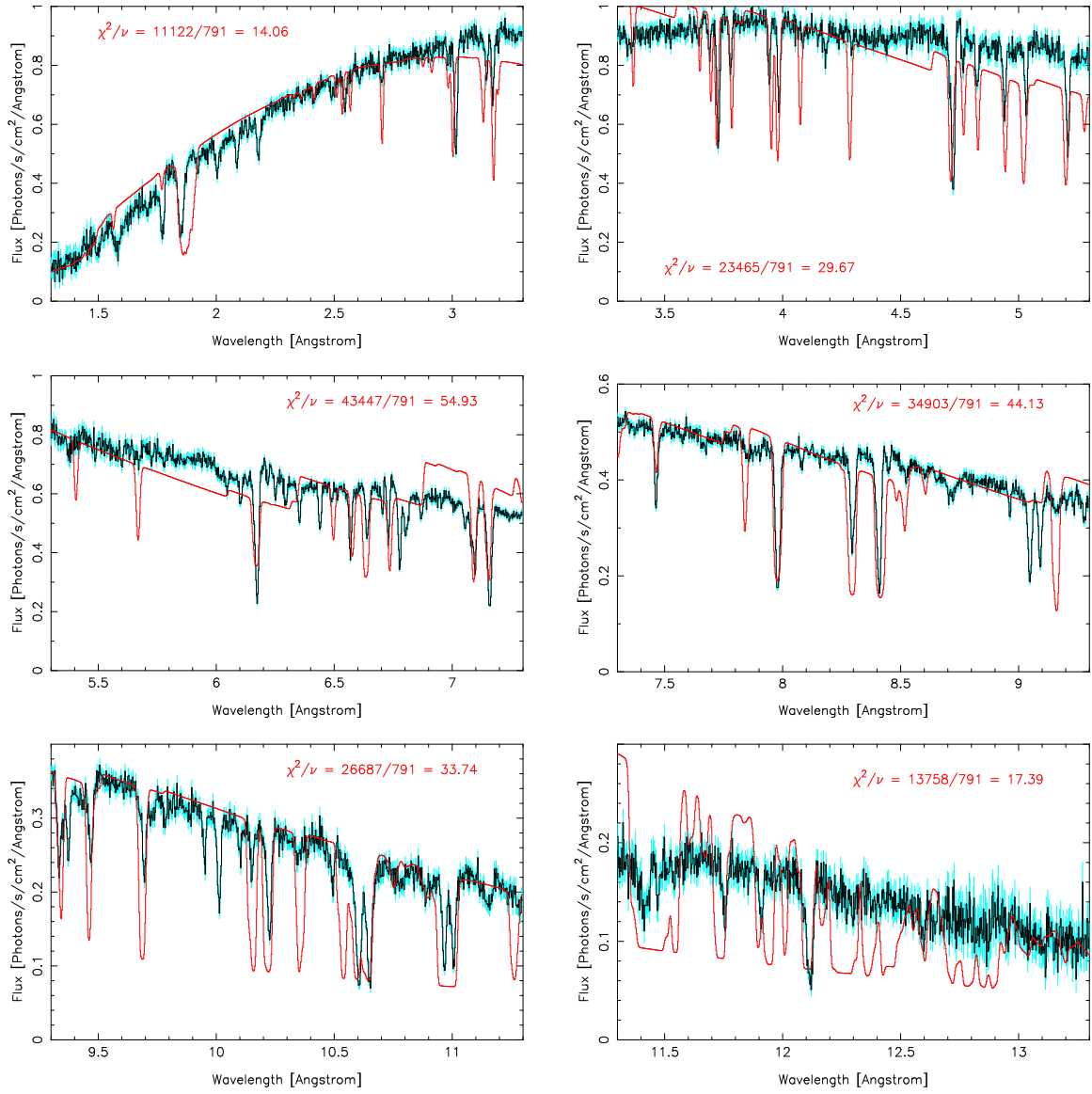


FIG. 10.— The plot above shows the disk wind spectrum of GRO J1655-40, fit in 2Å slices with an XSTAR model consistent with a thermally-driven wind (see models 1A and 3A in Tables 3 and 4). The model clearly fails to describe the spectrum in each wavelength slice. Apart from the ISM absorption and power-law index (fixed to the best-fit values from broad-band fitting with *RXTE*), the disk blackbody plus power-law continuum parameters were allowed to vary.

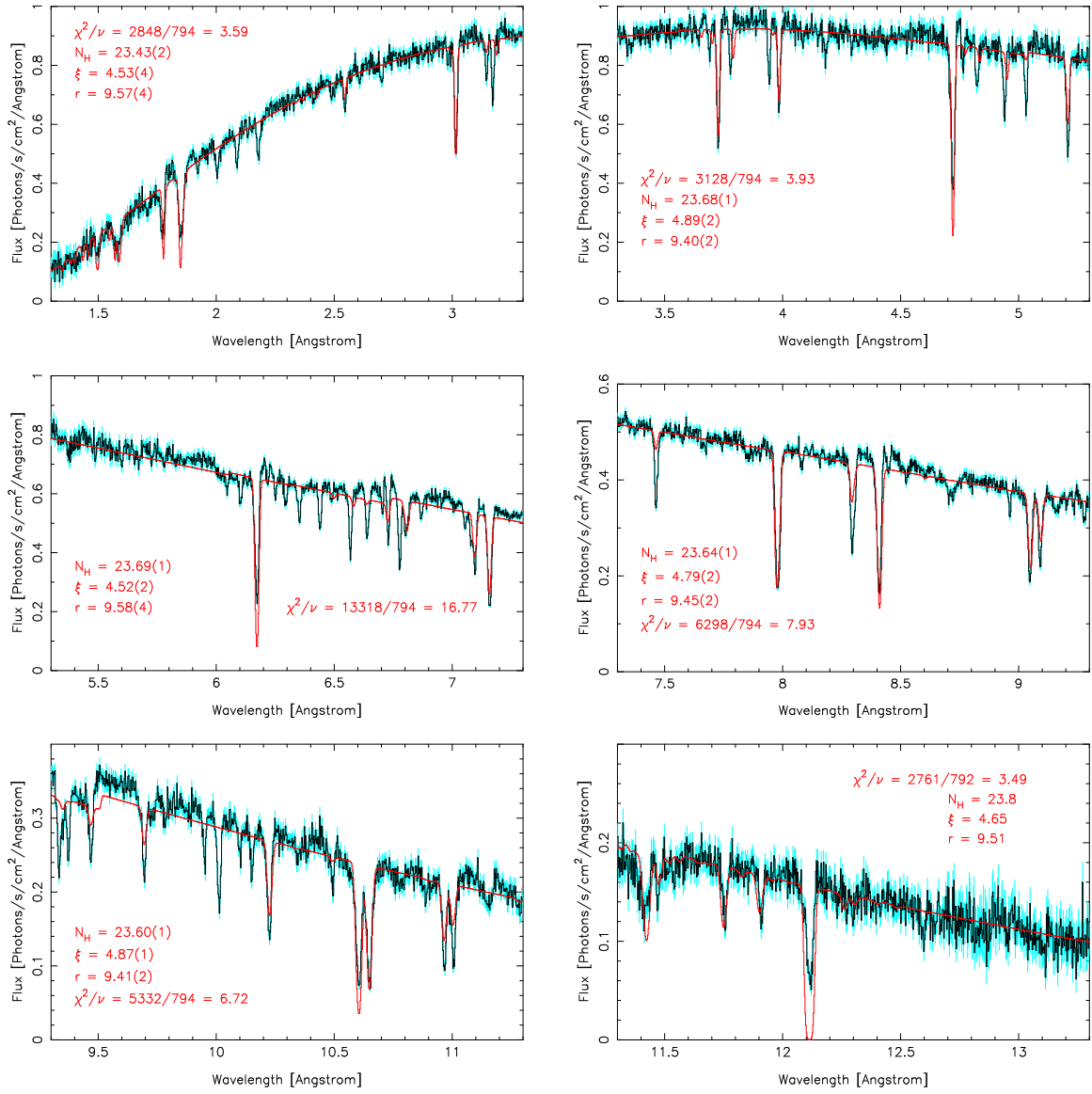


FIG. 11.— The plot above shows the disk wind spectrum of GRO J1655–40, fit in 2\AA slices with an XSTAR model allowed to vary in each segment. The absorption parameters derived from each fit are given in the panel where the spectrum and fit are plotted. In all segments, the parameters are consistent with a wind where magnetic driving is likely to be important. The XSTAR model depicted above is not a perfect description of the data, partially owing to the range of velocities in each segment; however, it is statistically far superior to the thermal wind model shown in Figure 10.

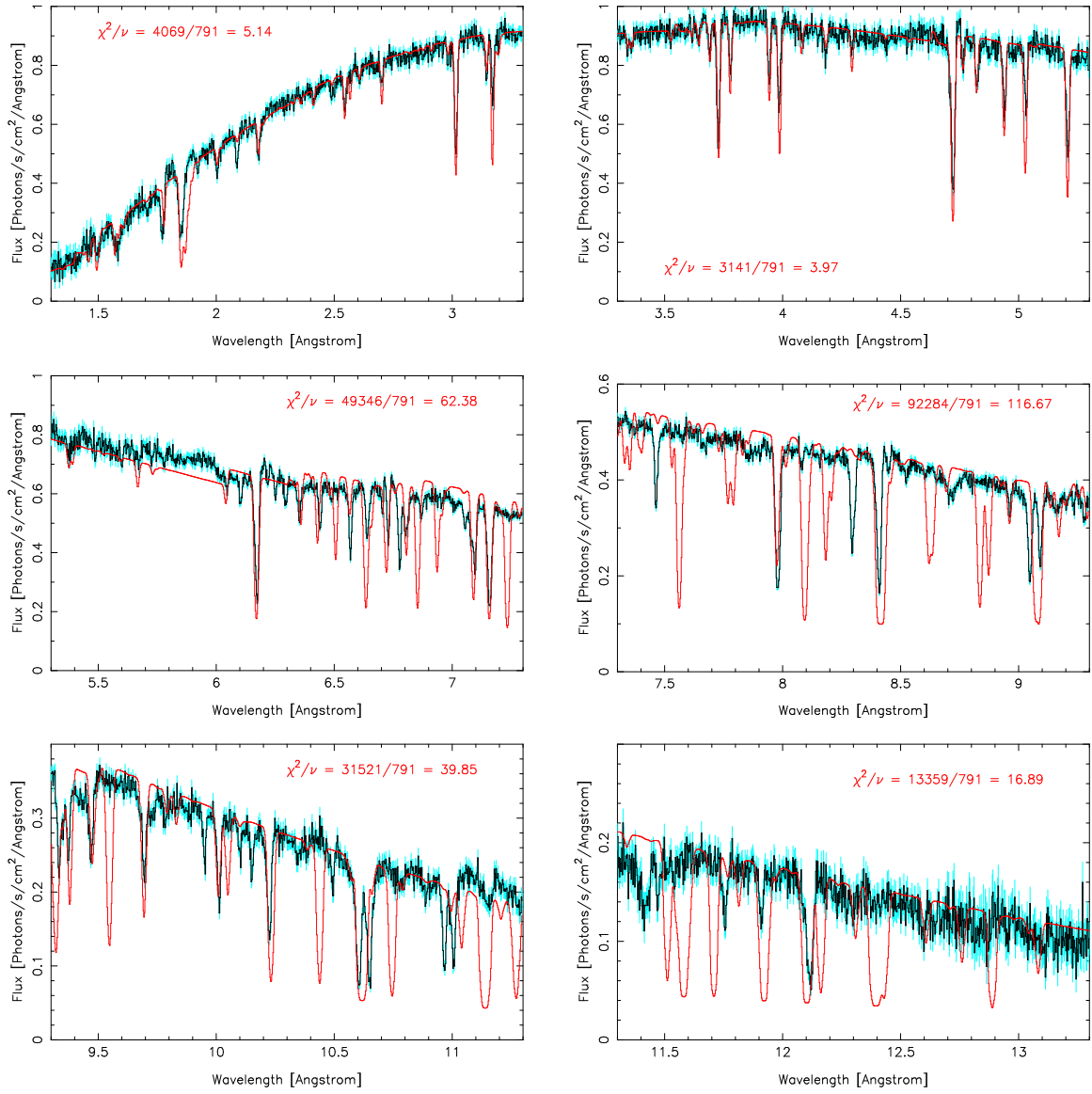


FIG. 12.— The plot above shows the disk wind spectrum of GRO J1655–40, fit in 2 Å slices with an Cloudy model consistent with a thermally–driven wind (see models 2A and 4A in Tables 3 and 4). The model clearly fails to describe the spectrum in each wavelength slice. Apart from the ISM absorption and power-law index (fixed to the best-fit values from broad-band fitting with *RXTE*), the disk blackbody plus power-law continuum parameters were allowed to vary.

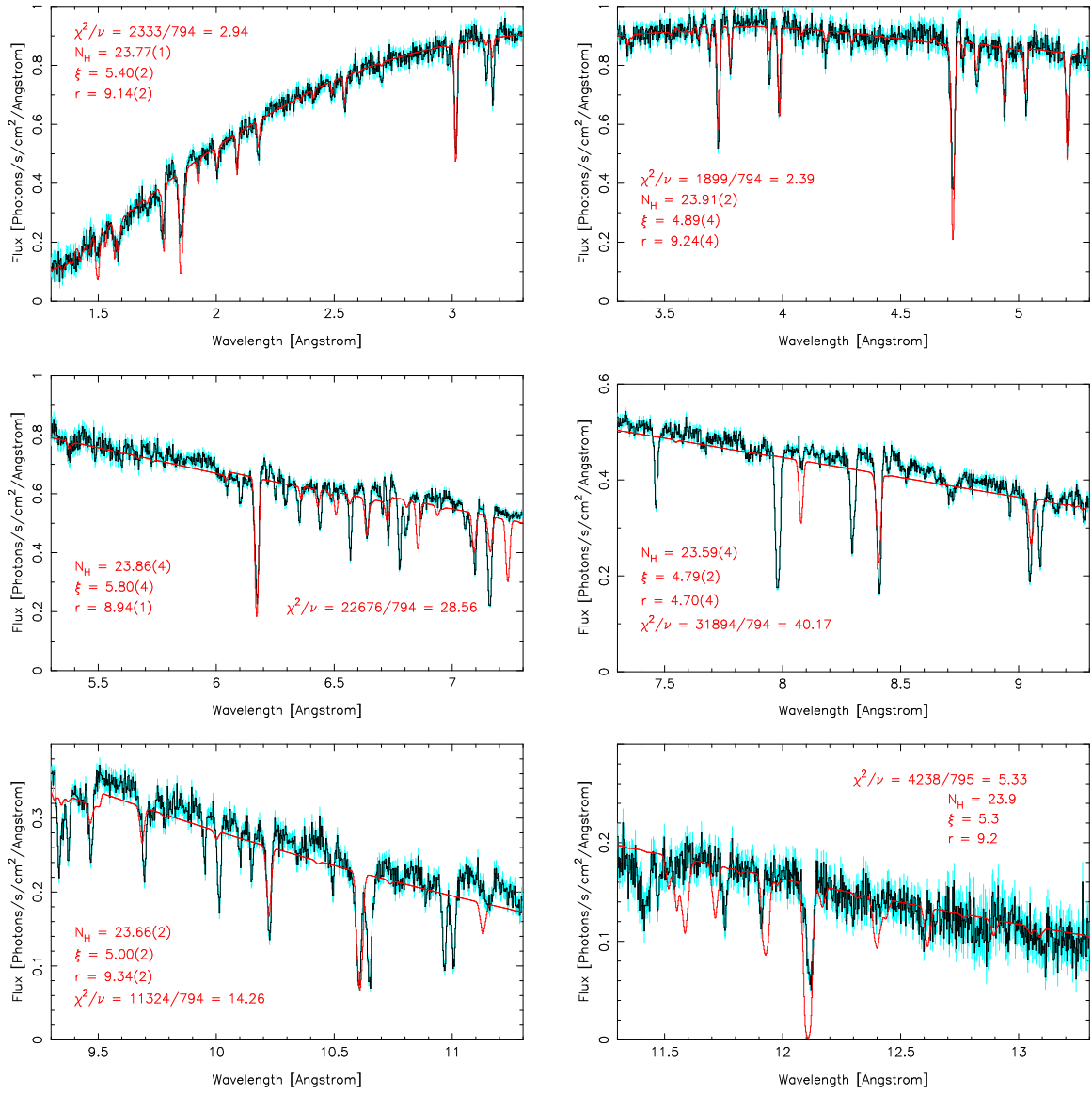


FIG. 13.— The plot above shows the disk wind spectrum of GRO J1655–40, fit in 2Å slices with a Cloudy model allowed to vary in each segment. The absorption parameters derived from each fit are given in the panel where the spectrum and fit are plotted. In all segments, the parameters are consistent with a wind where magnetic driving is likely to be important. The Cloudy model depicted above is not a perfect description of the data, partially owing to the range of velocities in each segment; however, it is statistically far superior to the thermal wind model shown in Figure 12.

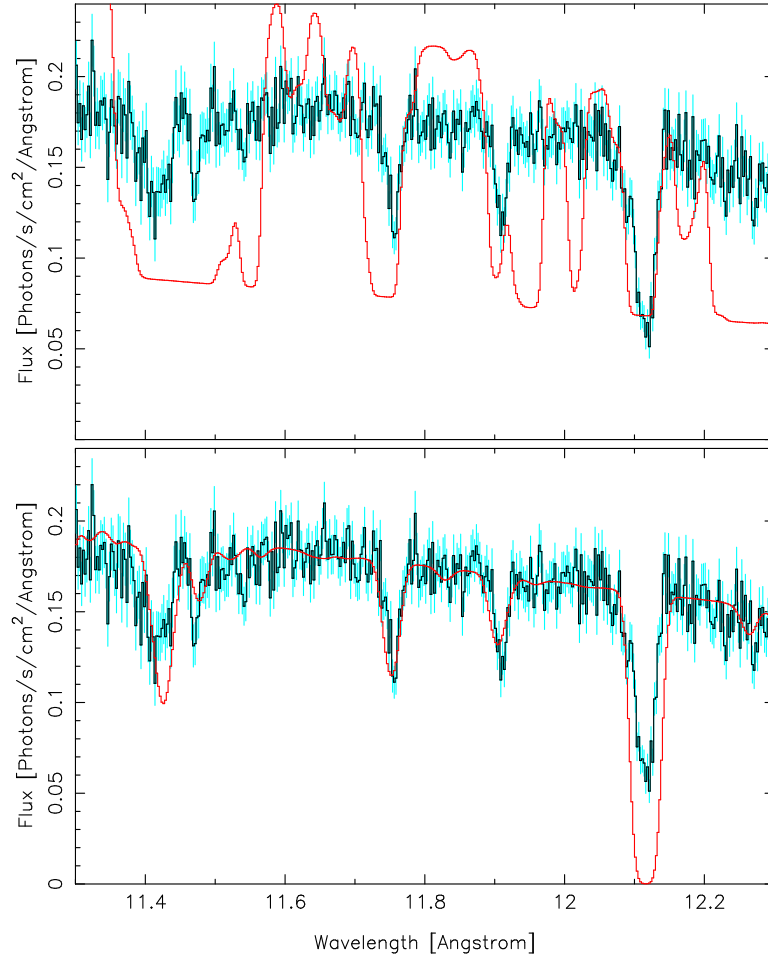


FIG. 14.— The plots above highlight fits to the density-sensitive Fe XXII lines at 11.77\AA and 11.92\AA . The models shown here are those depicted in Figures 10 and 11. The upper panel depicts a model consistent with a thermally-driven wind, based on the parameters given in Netzer (2006). The lower panel shows the best-fit XSTAR model for this region; in this model, the lines are well-represented and are clearly not saturated. These models strongly suggest that our estimate of the density ($\log(n) \simeq 13.7\text{--}14.0$) is robust. Cloudy models are not shown as the wavelengths for these ions appear to be incorrect, but it is clear in Figures 12 and 13 that our best-fit Cloudy models describe the data far better than alternative models.